Publications of the Astronomical Society of the Pacific, 132:104301 (19pp), 2020 October https://doi.org/10.1088/1538-3873/aba840

FEEDBACK: a SOFIA Legacy Program to Study Stellar Feedback in Regions of Massive Star Formation

N. Schneider[1], R. Simon[1], C. Guevara[1], C. Buchbender[1], R. D. Higgins[1], Y. Okada[1], J. Stutzki[1], R. Güsten[2], L. D. Anderson[3], J. Bally[4], H. Beuther[5], L. Bonne[6], S. Bontemps[6], E. Chambers[7], T. Csengeri[6], U. U. Graf[1], A. Gusdorf[8], K. Jacobs[1], M. Justen[1], S. Kabanovic[1], R. Karim[9], M. Luisi[3], K. Menten[2], M. Mertens[1], B. Mookerjea[10], V. Ossenkopf-Okada[1], C. Pabst[11], M. W. Pound[9], H. Richter[12], N. Reyes[2], O. Ricken[2], M. Röllig[1], D. Russeil[13], Á. Sánchez-Monge[1], G. Sandell[14], M. Tiwari[9], H. Wiesemeyer[2], M. Wolfire[9], F. Wyrowski[2], A. Zavagno[13], and A. G. G. M. Tielens[9,11]
[1] I. Physik. Institut, University of Cologne, Zülpicher Str. 77, D-50937 Cologne, Germany; nschneid@ph1.uni-koeln.de
[2] Max-Planck Institut für Radioastronomie, Auf dem Hügel 69, D-53121 Bonn, Germany
[3] Department of Physics and Astronomy, West Virginia University, Morgantown WV 26506, USA
[4] Center for Astrophysics and Space Astronomy, University of Colorado, Colorado 80309, USA
[5] Max Planck Institute for Astronomy, Königstuhl 17, D-69117 Heidelberg, Germany
[6] LAB, University of Bordeaux, CNRS, B18N, F-33615 Pessac, France
[7] USRA/SOFIA, NASA Ames Research Center, Moffett Field, CA 94035-0001, USA
[8] LPENS, LERMA, Université PSL, CNRS, Sorbonne Université, Université de Paris, Paris, France
[9] Department of Astronomy, University of Maryland, College Park, MD 20742, USA
[10] Tata Institute of Fundamental Research, Homi Bhabha Road, Mumbai 400005, India
[11] Leiden Observatory, Leiden University, PO Box 9513, 2300 RA Leiden, The Netherlands
[12] Institute of Optical Sensor Systems, DLR, Rutherfordstr. 2, D-12489 Berlin, Germany
[13] Aix Marseille Université, CNRS, CNES, LAM, Marseille, France
[14] Institute for Astronomy, University of Hawaii, 640 N. Aohoku Place, Hilo, HI 96720, USA
Received 2020 May 26; accepted 2020 July 20; published 2020 September 16

Abstract

FEEDBACK is a SOFIA (Stratospheric Observatory for Infrared Astronomy) legacy program dedicated to study the interaction of massive stars with their environment. It performs a survey of 11 galactic high mass star-forming regions in the 158 μm (1.9 THz) line of [C II] and the 63 μm (4.7 THz) line of [O I]. We employ the 14 pixel Low Frequency Array and 7 pixel High Frequency Array upGREAT heterodyne instrument to spectrally resolve (0.24 MHz) these far-infrared fine structure lines. With a total observing time of 96h, we will cover ~6700 arcmin^2 at 14.″1) angular resolution for the [C II] line and 6.″3 for the [O I] line. The observations started in spring 2019 (Cycle 7). Our aim is to understand the dynamics in regions dominated by different feedback processes from massive stars such as stellar winds, thermal expansion, and radiation pressure, and to quantify the mechanical energy injection and radiative heating efficiency. This is an important science topic because feedback of massive stars on their environment regulates the physical conditions and sets the emission characteristics in the interstellar medium (ISM), influences the star formation activity through molecular cloud dissolution and compression processes, and drives the evolution of the ISM in galaxies. The [C II] line provides the kinematics of the gas and is one of the dominant cooling lines of gas for low to moderate densities and UV fields. The [O I] line traces warm and high-density gas, excited in photodissociations regions with a strong UV field or by shocks. The source sample spans a broad range in stellar characteristics from single OB stars, to small groups of O stars, to rich young stellar clusters, to ministarburst complexes. It contains well-known targets such as Aquila, the Cygnus X region, M16, M17, NGC7538, NGC6334, Vela, and W43 as well as a selection of H II region bubbles, namely RCW49, RCW79, and RCW120. These [C II] maps, together with the less explored [O I] 63 μm line, provide an outstanding database for the community. They will be made publically available and will trigger further studies and follow-up observations.

Key words: Giant molecular clouds – Astronomical instrumentation – H II regions – Interstellar clouds – Interstellar filaments – Molecular clouds – Observatories – Stellar wind bubbles – Submillimeter astronomy

Online material: color figures

1. Introduction

The interaction of massive stars with their environments regulates the evolution of galaxies. Mechanical and radiative energy input by massive stars stir up and heat the gas and control cloud and intercloud phases of the interstellar medium (ISM). Stellar feedback also governs the star formation efficiency of molecular clouds (Elmegreen 2011; Hopkins et al. 2014). On the

one hand, stellar feedback can lead to a shredding of the nascent molecular cloud within a few cloud freefall times thereby halting star formation (Matzner 2002; Geen et al. 2016; Kim et al. 2018). The efficiency of this process is somewhat controversial as some models (Dale et al. 2014), combining effects of photoionization and momentum-driven winds, conclude that the effectiveness of stellar feedback to disperse a cloud is small. A recent observational study of Watkins et al. (2019) argues similarly, proposing that feedback does not influence dense gas and that the cloud morphology and average density at the time when the first O-stars form is decisive for the star formation efficiency. On the other hand, it has been proposed that massive stars can also provide positive feedback to star formation as gravity can more easily overwhelm cloud-supporting forces in swept-up compressed shells (Elmegreen & Lada 1977). A popular observational example for such a triggering of star formation is RCW120 (Deharveng et al. 2010; Zavagno et al. 2010). But again, this scenario was challenged by Walch et al. (2015) who propose a hybrid form of triggering, which combines elements of collect & collapse (Elmegreen & Lada 1977) and radiation driven implosion (Bertoldi 1989; Lefloch & Lazareff 1994) models.

Separate from the issue of how stellar feedback impacts star formation, it is evident that stars control the radiative energy budget of the ISM and its emission characteristics. Extreme ultra-violet (EUV) photons from massive stars with energies >13.6 eV ionize hydrogen, creating H II regions that cool through H recombination lines and forbidden, collisionally excited transitions of trace elements. Less energetic photons photodissociate molecules and photoionize species such as carbon (C) and sulfur (S). These far-UV (FUV) photons heat the gas through photoelectrons from large Polycyclic Aromatic Hydrocarbon (PAH) molecules and very small grains, and by collisional de-excitation of vibrationally excited H_2 molecules, while it cools predominantly through far-infrared fine-structure lines of ionized carbon (C^+) and atomic oxygen (O). The result is a Photo Dissociation Region (PDR): a layer of warm, atomic and molecular gas that separates the ionized gas from the surrounding molecular cloud material (Hollenbach & Tielens 1999). The physical properties of PDRs are largely controlled by the coupling of the FUV photons to the energy budget of the gas. Detailed models have been developed for this coupling (Bakes & Tielens 1994) but as the properties of large molecules and very small grains are not well known, these models are uncertain. Observational characterization of the heating efficiency of FUV photons has hitherto only been possible for a handful of sources (Okada et al. 2013; Pabst et al. 2017). This uncertainty in the heating of the gas enters directly into PDR models (Kaufman et al. 2006; le Petit et al. 2006; Röllig et al. 2006, 2007; Pound & Wolfire 2008) that are widely used to analyze observations and, as a result, the derived physical properties carry a large systematic uncertainty.

Another source of ionization and heating must be considered when massive stars are present. These are X-rays, produced when the fast stellar wind of OB stars shocks the surrounding medium (Weaver et al. 1977). Molecular gas exposed to X-rays has a different chemical structure and thermal balance than PDRs. These X-ray dominated regions (XDRs) span a temperature range of $\sim$200 K to 10^4 K and produce large column densities of warm gas (Maloney et al. 1996). In general, the mechanical luminosity of the stellar wind is only a small ($\sim 10^{-3}$) fraction of the radiative luminosity and the X-ray luminosity is only a small ($\sim 10^{-4}$) fraction of the mechanical luminosity (most of the cooling goes through adiabatic expansion). Hence, X-rays will probably not affect significantly the typical PDR cooling lines ([C II], [O I], low to mid-J CO). Modeling emission lines arising in PDRs and XDRs (Meijerink et al. 2006; Spaans & Meijerink 2008) predict that high-J CO lines are good XDR tracers. However, high density, high temperature PDR models also succeed in explaining observed CO line fluxes (Stock et al. 2015). In order to separate the PDR contribution to XDR diagnostic tracers requires a deep understanding of the physics of FUV heated gas and its cooling response.

Cosmic Rays (CRs) represent yet another channel of feedback exerted from stars on the ISM of galaxies. The bulk of the mid-energy ($\sim$1 GeV) CRs is thought to be originating from supernova (SN) explosions and supernova remnants (Bykov et al. 2018), but the idea that large (typically >10 pc) superbubbles could contribute significantly to the Galactic CR budget has recently emerged (Tatischeff & Gabici 2018). Though most of CRs quickly diffuse away, they may still play a role in the FUV shielded H II region/molecular cloud interface (Meng et al. 2019; Padovani et al. 2019). We will thus make effort to consider and study the impact of CRs on the immediate environment of massive stars.

Through their winds and explosions, massive stars impact the ISM dynamically on all scales. Turbulence is driven on the sub-parsec scale by radiation pressure and jets and outflows, but can also be generated Galaxy-wide by supernovae explosions. This injection of mechanical energy into the ISM is the origin of the Hot Intercloud Medium (HIM) and a source of turbulent pressure that supports the gas disk and the clouds therein against self-gravity and gravitational collapse in the host galaxy's potential (McKee & Ostriker 1977). At intermediate scales (up to a few tens of parsec), radiation pressure and winds sweep up gas into "bubbles," i.e., ring- or shell-like structures. Surveys such as the mid-IR Galactic Legacy Infrared Mid-Plane Survey Extraordinaire (GLIMPSE) have revealed that these bubbles are ubiquitous morphological features in the ISM of the Milky Way (Churchwell et al. 2006) and enclose H II regions (Deharveng et al. 2009). They may be caused by the thermal expansion of H II regions driven by the overpressure of ionized gas, by the mechanical action of stellar winds from massive stars creating X-ray emitting hot gas, and by the effects of radiation pressure on surrounding dust and gas (Stroemgren 1939; Spitzer 1968; Weaver et al. 1977; Draine

2011; Haid et al. 2016). However, it is not settled whether these bubbles are indeed 3D structures. In the plane of the sky, they resemble ring-like structures but this geometry might largely reflect projection effects (Beaumont & Williams 2010; Kirsanova et al. 2019). Recent [C II] observations of the Orion molecular cloud, on the other hand, clearly reveal 3D expanding shell structures associated with the areas of active star formation, M42, M43, and NGC 1977 (Pabst et al. 2019, 2020).

Not all H II regions have a bubble morphology. In particular massive star-forming giant molecular cloud complexes such as the Cygnus X region or W43 are a mixture of individual bubble-like H II regions and a more inhomogeneous distribution of ionized gas in which the cool molecular gas is pervaded by a web of filaments and larger clouds. Under the influence of ionizing radiation, a rich diversity of structures such as pillars, bright-rimmed clouds and globules are created at the H II region/molecular cloud interface. These features have long been observed at various wavelengths (Herbig 1974; Schneps et al. 1980; Hester et al. 1996; White et al. 1997; Schneider et al. 2016), but it is mostly unexplored how radiation and stellar wind impact filaments and massive cloud ridges, and how that influences subsequent filament/cloud evolution and star formation. So far, it is known, thanks to far-infrared dust imaging surveys by Herschel, that filaments play an important role in the molecular cloud- and star formation process (André et al. 2010; Hennemann et al. 2012; Hill et al. 2012b; Schneider et al. 2012a). Simulations performed by Inutsuka et al. (2015) show that molecular clouds can form due to multiple compressions by overlapping dense shells driven by expanding bubbles. Filaments are then the first step of this formation process, i.e., the compressed shell, as was proposed in a recent study of the RCW120 bubble (Zavagno et al. 2020). Summarizing, detailed studies of both small, bubble-like H II regions and large cloud complexes are required to probe the underlying physical processes, the structure and physical properties of the ambient ISM into which they are expanding, the hydrodynamical response of gas in the ISM to stellar action, and the radiative coupling of gas and dust to the intense photon fields of massive stars.

The efficient mapping capabilities of ground based sub-mm wavelength radio-telescopes, the upGREAT array receiver on SOFIA, and (F)IR imaging from Spitzer, WISE, and Herschel has now enabled in depth studies of the coupling between molecular clouds and OB stars. In particular the [C II] $^2P_{3/2}$–$^2P_{1/2}$ fine-structure line at 157.74 μm or 1.90054 THz ($E/k_b = 91.2$ K) offers a unique probe of the radiative and kinetic interaction of massive stars with their environment. The C^+ ion is the dominant form of carbon in atomic hydrogen and CO-dark molecular gas layers because it has a low ionization potential of 11.3 eV, slightly below the ionization potential of hydrogen which is 13.6 eV. The [C II] line is the dominant cooling line of PDR surfaces of FUV illuminated molecular clouds where stellar photons dissociate molecular gas and heat it to temperatures of $T \sim 200$ K. The line is easy to excite thermally by collisions with electrons, atomic hydrogen and molecular hydrogen. The critical density, defined by the collisional de-excitation rate being equal to the effective spontaneous decay rate, depends on the temperature. It is 9 cm^{-3}, 3×10^3 cm^{-3}, and 6.1×10^3 cm^{-3} for collisions with e^-, H and H_2, respectively, for gas temperatures $\lesssim$100 K (Goldsmith et al. 2012).

The [O I] line at 63.18 μm or 4.74478 THz ($E/k_b = 228$ K) is the most important cooling line for warmer $T > 200$ K and denser gas with a critical density of 5×10^5 cm^{-3} for collisions with H_2 (Röllig et al. 2006). The ratio of [C II] to [O I] line fluxes depends on the temperature and density of the gas.

In massive star-forming regions, energy is also injected in the form of shocks (expanding ionization fronts, stellar winds) so that in particular the [O I] observations also need to be interpreted in the context of irradiated shock models, where the effects of FUV photons on the physical conditions and chemistry of the region are included. For understanding the dynamics of the gas emitting the [C II] 158 μm line, it is also important to carefully study the line profile in order to assess possible optical depth effects. Recent studies (Graf et al. 2012; Ossenkopf et al. 2015; Mookerjea et al. 2018, 2019) have shown that the [C II] line is often optically thick and shows self-aborption effects. The [^{12}C II] optical depth can be estimated when the [^{13}C II] hyperfine structure (hfs) satellite emission is detected (Ossenkopf et al. 2013; Okada et al. 2019; Guevara et al. 2020).

The SOFIA legacy program FEEDBACK is designed to probe the radiative and mechanical interaction of massive stars with their natal clouds. The focus is on understanding how massive stars control star formation, to what extent they disrupt molecular clouds, how turbulence is injected into the ISM, if and how new star formation can be triggered, and how their FUV photons couple to atomic and molecular gas in the surrounding PDRs. With the 14 pixel Low Frequency Array (LFA) upGREAT heterodyne spectrometer, we efficiently observe over large scales (several 1000 arcmin^2) and at high spatial (14.1″) and high spectral (0.24 MHz) resolution a statistically significant sample of Galactic star-forming molecular clouds. In parallel, the 4.7 THz High Frequency Array (HFA) channel of upGREAT delivers maps of the [O I] 63 μm line, which provide the community with unique complementary data in the context of PDR and shock modeling. These latter maps are undersampled because the focus was on [C II] mapping, but were observed in a regular mapping scheme (Section 4).

In order to prepare the community for the opportunities offered by the FEEDBACK project and to allow them to

prepare ancillary observations, we outline the goals of the project (Section 2) and describe the source selection (Section 3). The planning of the observations, performance and data reduction is presented in Section 4. First results from SOFIA cycle 7 observations are given in Section 5. In Section 6 we outline which data products will be delivered to the community and Section 7 summarizes the paper.

2. Goals—FEEDBACK Key Science

Investigating the effects of stellar feedback from massive stars is a vast science topic but we reduce it here to these questions: (1) How large is the kinetic energy input into the ISM and, connected to this, how does the surrounding medium react? (2) How does the radiative coupling of interstellar gas to the FUV photons work and how does the gas respond? We specifically address these subjects by mapping the [C II] 158 μm and [O I] 63 μm lines in Galactic massive star-forming regions and, thus, focus in the following on how these observations help to assess stellar feedback effects.

2.1. Morphology and Dynamics

Infrared (IR)- and FIR-surveys of the Milky Way, carried out with Spitzer, WISE, and Herschel, and radio surveys, have revealed many thousand H II regions (Paladini et al. 2003; Churchwell et al. 2006; Deharveng et al. 2010; Anderson et al. 2011, 2014). Anderson et al. (2011) have shown that approximately half of all H II regions have a ring-like morphology, commonly referred to as "bubbles." For the other H II regions, their geometry varies between bipolar structures and more complex regions with fragmented shells, pillars, and globules.[15] Within FEEDBACK, we observe template regions for these different geometries over a large range of size scales (from a few pc to tens of pc).

In the classical view of Spitzer (1968), expanding H II regions, excited by massive stars, sculpt ionized spherical cavities in their surrounding molecular clouds. Because stellar radiation both ionizes and heats gas up to $\sim 10^4$ K, it creates a strong overpressure that expands the gas into the surrounding cold molecular cloud. For homogeneous initial conditions, this expansion can be described by a simple analytical solution (Spitzer 1968). For very massive stars, stellar winds are important as well since they drive shocks into the surrounding medium, creating XDRs with temperatures up to 10^4 K in regions with high gas column density and—in the fully ionized phase—a hot, but very tenuous, plasma with a typical density of $n \sim 1$ cm^{-3} and temperatures up to 10^6 K. The resulting overpressure of this plasma leads to the formation of dense swept-up shells on the surfaces of surrounding clouds (Weaver et al. 1977). The inside of this shell is ionized by the stellar EUV photons, while the shell forms a dense PDR. Energy conduction from the hot plasma to the dense shell across the contact discontinuity that separates the two, results in additional cooling, as well as mass loading of the plasma. While this process is not well understood, it likely controls the dynamics of the shell. Finally, radiation pressure on the dust and gas assists the expansion, or even dominates under extreme conditions (Krumholz & Matzner 2009; Draine 2011; Haid et al. 2016). Note that stellar wind is not the only way to have a shock because the expansion velocity of the ionized gas into the surrounding medium is supersonic. The shock front precedes the ionization front as the expansion continues and the surrounding material is locked into a layer (between the shock front and the ionization front). In simulations (Dale et al. 2014), the wind-blown H II regions resemble better observed H II region morphologies than those created by ionization alone. More specific, the relative effects of stellar winds are strongest at early times when the massive star(s) are embedded in dense gas from the molecular cloud. Once this gas has been cleared away, the expanding H II region dominates the dynamical and morphological evolution of the cloud. It is one of the main objectives of FEEDBACK to discern if H II regions are wind-driven or ionization-driven, or both, depending on physical parameters such as density, radiation field and spectral type(s) and ages(s) of the exciting star(s).

Each of these mechanisms leads to the creation of a dense shell of gas and the density profile along a cut orthogonal to the ionization front will be asymmetric, with a sharp gradient toward the H II region. Such profiles were indeed observed, using for example Herschel dust column density maps (Peretto et al. 2011; Schneider et al. 2013; Tremblin et al. 2013, 2014). The PDR is typically trapped in this shell and its contribution will dominate the [C II] line emission. Hence, we can assess the distribution and the dynamics of the warm PDR gas via the [C II] line, while low- to mid-J CO lines trace the molecular gas further away from the ionization front as well as the surrounding unperturbed cold molecular cloud material, see, e.g., Peng et al. (2012), Mookerjea et al. (2012), Stock et al. (2015), Nagy et al. (2017), Joblin et al. (2018), Schneider et al. (2018). The high angular and spectral resolution data of the [C II] line will reveal the distribution and velocity field of the PDR material. Some of the [C II] emission may originate in the the H II region itself and this will have to be distinguished through various diagnostics. First, the [C II] emission distribution, velocity field and line width need to be compared to other data sets, i.e., with diffuse X-ray emission, molecular line data, dust column density and temperature maps. Position-velocity (pv) diagrams and channel-maps of [C II] will show signatures of near and far molecular walls if the bubbles are 3D shells. Evaluating the energetics, [C II] observations will also show whether such a [C II] bubble expands due to the impact of stellar winds or the pressure-driven expansion of the H II region. In addition, the contribution of strong stellar winds can be assessed by X-ray emission. Several of our targets have been

[15] See also the "The Milky Way Project" (Simpson et al. 2012) catalog of bubbles (Beaumont et al. 2014; Jayasinghe et al. 2019), based on Spitzer.

observed by Chandra in the MOXC surveys and show diffuse X-ray emission, tracing stellar wind activity (Townsley et al. 2014, 2018, 2019).

Accompanying observations of CO and/or other molecular lines tracing the molecular cloud will then show how such an expansion continues in the cold and denser gas phase. However, disentangling the primordial cloud structure and the effects of winds and photoionization carving into the clouds will be a challenge (see also Section 2.2). Line profiles of [C II] are fitted using multicomponent Gaussians to determine surface brightness and identify coherent velocity and cloud structures/components from the channel and pv maps. Because of the high sensitivity of our data, we are able to detect the [^{13}C II] hfs emission in many sources. This allows by comparison of the line profiles study of whether the [C II] line is affected by self-absorption and thus might mimic unreal kinematics.

A recent [C II] study of the Orion molecular cloud (Pabst et al. 2019, 2020) displays clear observational signatures of several expanding structures. The Veil nebula dominates the large scale appearance of the region. Over the last ~100,000 yr, the stellar wind from the massive O7 star θ^1 Orionis C has blown a 4 pc diameter half sphere containing some 2000 $M_\odot$ of gas expanding at 15 km s^{-1} toward the low pressure region in front of the OMC1 core. The cavity of the shell is filled by hot plasma from the shocked stellar wind (Güdel et al. 2008). The total kinetic energy of this expanding half-shell is comparable to the total mechanical energy delivered by the wind. The [C II] observations of the Orion Molecular cloud also reveal expanding shells surrounding M43 and NGC1977. In these two cases, the overpressure in the ionized gas, created by these B0.5 stars, gives rise to a Spitzer-type expansion (Pabst et al. 2020).

2.2. Triggering of Star formation

The [C II] observations form the basis for a study on the dynamical response of newly formed stellar clusters and the disruption of their nascent clouds. Dense gas condensations, i.e., the locations of future stars, might form as a result of fragmentation of the neutral material due to the gravitational instability during the expansion of the H II region. These cold, dense cores in the H II region/molecular cloud interface of the FEEDBACK sources can be traced by submm dust continuum observations, either already performed by Herschel (Liu et al. 2017; Tigé et al. 2017; Zhang et al. 2020), or using ground-based instruments such as ArTéMiS (Hill et al. 2012a; André et al. 2016; Zavagno et al. 2020) or LABOCA (Massi et al. 2019) and—for detailed studies—ALMA and NOEMA.

So far, an overdensity of young stellar objects is observed at the edges of H II regions, and up to 25% of the ionized regions show high-mass star formation triggered on their edges (Deharveng et al. 2010; Thompson et al. 2012). In the picture of sequential triggered star formation (Elmegreen & Lada 1977), there should be an age gradient observed in the spatial distribution of young sources in the surrounding molecular cloud (Martins et al. 2010). Furthermore, radiative feedback will impact gas and dust temperatures within the molecular cloud, modifying the initial conditions for collapse and affecting proto- and young stellar objects in different evolutionary phases. However, observational studies of this issue are inconclusive. Taking the example of the Rosette Molecular cloud, Balog et al. (2007) reveal an increase of the average NIR excess fraction for stellar clusters with distance to the cluster center, and Williams et al. (1994) show that star formation activity is more intense in the H II region/molecular cloud interface region than in the molecular cloud center. On the other hand, Roman-Zuniga et al. (2008) and Cambrésy et al. (2013) found that the relative age differences of the clusters are not consistent with a sequential triggered star formation scenario. Schneider et al. (2012a) argue that star formation takes place in filaments and filament mergers that arose from the primordial turbulent structure but can be locally induced in the direct interaction zone between an expanding H II region and the molecular cloud.

The [C II] data, combined with molecular observations, will provide physical conditions, and in particular pressures in these regions and will help to evaluate if triggered star formation can occur in dense, swept up shells (Section 2.3). This will be a difficult task but we will for example investigate the variation of the [C II] and molecular line velocities and line widths from the interface region into the surrounding cloud. Clumpiness of the cloud needs to be taken into account because it enables UV radiation to penetrate deeper into the cloud, giving rise to [C II] emission from many PDRs along the line-of-sight. Herschel data provide the distribution of the dust temperature that will be compared to the gas temperature, derived from CO.

2.3. Kinetic and Radiative Energy

The amount of energy and momentum that drive the dynamics of H II regions need to be evaluated for each source in order to assess which mechanism is the dominant process for each source. Pellegrini et al. (2007, 2011), Lopez et al. (2011, 2014) for example provide a comprehensive overview how the pressure (or energy) terms for direct radiation, dust-processed IR radiation, warm ionized gas, and hot, shock-heated by stellar winds are determined observationally. We here focus on how [C II] and [O I] observations, together with complementary data, can be used for estimating the energy budget.

The kinetic energy input into the ISM by massive stars will be investigated as a function of star formation activity (cluster size, spectral type, stellar wind) and evolutionary stage of the region both in terms of the generation of large scale motions as well as the local injection of turbulence into molecular clouds. The [C II] observations reveal the morphology of expanding

structures, and their masses are determined from the [C II] column density and compared to the molecular gas mass, estimated from Herschel dust column density maps and CO maps. The [C II] line can be affected by high optical depth, so that mass estimates are lower limits, but observations of the optically thin [^{13}C II] hfs emission can be employed. The integrated intensity of the [^{13}C II] hfs emission is expected to be only a few percent of the [^{12}C II] emission (typically 50 times lower), depending on the elemental $^{12}C/^{13}C$ abundance ratio and the optical depth of the emission in the main isotope. However, averaging over a large area, the Signal-to-Noise ratio (S/N) of the [^{13}C II] hfs emission can be sufficiently increased to derive the optical depth and hence a lower limit on the mass of emitting gas. For shells expanding toward us, extinction measurements of the stars in the ionized gas can also provide an estimate of the column density through the shell and, hence, its mass. Combined with the measured expansion velocity, this yields the kinetic energy of the gas, which can be directly compared to the thermal energy of any hot plasma present (determined from X-ray observations) and of the ionized gas. The ionizing photon flux and the total luminosity of the region are estimated from optical, radio, and IR observations. The spectral types of the ionizing stars in each cluster have been determined directly through infrared spectroscopy. Hence, we can observationally link the kinetics of the shell to the stellar characteristics (wind mechanical energy, luminosity).

We can also quantify the radiative coupling of PDR gas to the FUV photons. [C II] line intensities are directly compared via correlation plots to CO emission, IRAC 8 μm and WISE 12 μm emission due to PAHs, and PACS 70, 160 μm (and 100 μm if available) far-IR dust emission, all convolved to the same beam size. The [C II] line is the dominant cooling line of the gas and by comparing the integrated line intensity to the total infrared dust and PAH emission we empirically derive the heating efficiency in terms of the [C II]/FIR (or [C II]/TIR[16]), [C II]/CO and [C II]/PAH emission ratios (see Okada et al. 2013; Pabst et al. 2017; Anderson et al. 2019). Theoretically, the heating efficiency depends on the ionization parameter, $\gamma = G_0 T^{1/2}/n_e$ with G_0 the intensity of the radiation field in terms of the average interstellar radiation field, T the gas temperature and n_e the electron density (Bakes & Tielens 1994). As PAHs and grains charge up (large γ), the ionization potential increases and fewer photons can further ionize the PAHs/grains. Moreover, the photoelectron has to overcome an increased Coulomb potential, diminishing the energy delivered to the gas. Hence, in a stronger radiation field or lower density region, PAHs and very small grains charge up and the heating efficiency drops. Presently, there is limited data available (Okada et al. 2013; Pabst et al. 2017), showing a decrease with ionization parameter as theory predicts. However, overall, theory seems to overpredict the heating efficiency. Preliminary analysis of the Orion data reveals a large spread in heating efficiency at any given ionization parameter. These variations seem to be linked to the spatial location in the region, indicating a dependence on local conditions not caught by the ionization parameter, or on the past evolution of the region.

FEEDBACK also has the potential for follow-up studies of γ-ray emission from highly dynamic and ionized regions of the ISM. Several of our targets show energetic γ-ray emission, detected with Fermi and/or HESS. These are Cygnus X, observed with Fermi (Ackermann et al. 2011), RCW49 with HESS (Aharonian et al. 2007; HESS Collaboration et al. 2011), and W43 with Fermi (Lemoine-Goumard et al. 2011) and HESS (Chaves et al. 2008). M16, M17, and RCW36 are listed in the Fermi Large Area Telescope Fourth Source Catalog (4FGL, Abdollahi et al. 2020).

2.4. Photodissociation Regions

The coupling of FUV photons to the gas is a key process that sets the structure and physical conditions in PDRs and their emission characteristics (Hollenbach & Tielens 1999), and regulates the phase structure of the ISM (Wolfire et al. 1995, 2003). The FEEDBACK program allows in depth studies of the structure and characteristics of PDRs on small ($\sim$1 pc) and large (tens of pc) physical scales. The [C II] line is also an important coolant of warm neutral atomic and CO-dark (Wolfire et al. 2010) molecular gas in PDRs and the cloud selection spans a wide range of physical conditions that are well probed by [C II]. The (undersampled) [O I] 63 μm maps will be bright in the densest regions illuminated by strong FUV fields. We are also obtaining complementary data in other PDR tracers, namely the [C I] line at 490 GHz, using the 4GREAT receiver on SOFIA and the APEX telescope, and mid- to high-J CO lines using APEX. We sample a wide range of physical conditions including the radiation field (G_0 ranging up to a few times 10^5), (electron) density (typically from 10^2 to 10^6 particles cm^{-3}), gas temperature (from 10^2 to 10^3 K), and spectral type of the illuminating star (O9 to O4 and WR).

In order to enable a more efficient way to compare [C II] and [O I] maps with PDR models, we are upgrading the PDR Toolbox (Kaufman et al. 2006; Pound & Wolfire 2008) at http://dustem.astro.umd.edu/pdrt. The PDR code used to generate its underlying database of line intensities has improved physics and chemistry. Critical updates include those discussed in Neufeld & Wolfire (2016), plus photorates from Heays et al. (2017), oxygen chemistry rates from Kovalenko et al. (2018), and Tran et al. (2018), and carbon chemistry rates from Dagdigian (2019). We have also implemented new collisional excitation rates for [O I] from Lique et al. (2018) (and Lique private communication) and have included ^{13}C chemistry along with the emitted line intensities for [^{13}C II] and ^{13}CO. The new PDR Toolbox covers many more spectral lines

[16] TIR is the total infrared flux between 3 and 1100 μm (Dale & Helou 2002), while FIR is the total FIR flux between 42.5 and 122.5 μm (Helou et al. 1988).

and metallicities and allows map-based analysis so users can quickly compute spatial images of density n and radiation field G_0 from map data. It has been rewritten in Python and provides Jupyter notebooks for data analysis. It also can support other PDR model codes such as KOSMA-τ (Röllig et al. 2006), enabling comparison of derived properties between codes.

KOSMA-τ differs from all other numerical PDR codes in that it is simulating the PDR emission from a spherical model cloud. This allows to model a wider range of astrophysical scenarios compared to plane-parallel geometries. A superposition of many small clumps can represent the inhomogeneous structure of the interstellar medium, while the limit of large clumps approaches the plane-parallel picture. Stutzki et al. (1998) showed that the fractal nature of the interstellar medium can be represented by an ensemble of clumps following a well-defined size distribution. This allows us to successfully model the highly structured PDRs in our observational sample by the superposition of individual spherical model clouds. KOSMA-τ was compared against other models in a dedicated benchmark study in 2007 (Röllig et al. 2007) and the code is continuously updated and improved as new data (e.g., reaction rates, atomic and molecular data) become available. Recent updates particularly refined the chemistry module of the code, including:

1. Flexible inclusion of isotopomeric chemistry.
2. Improved treatment of linear and cyclic isomers of a given molecule.
3. Inclusion of exothermal reaction energies as heating terms in the local energy balance.
4. New solution algorithms in order to improve numerical stability.
5. Introduction of full surface chemistry.
6. Inclusion of time-dependent numerical solvers.

A detailed description of the current state of the code is in preparation (M. Röllig et al. 2020, in preparation). Presently we are working to incorporate non-local transport terms such as diffusion and advection into the code framework. Moreover, we expand the three-dimensional modeling capabilities of KOSMA-τ-3D (Cubick et al. 2008; Andree-Labsch et al. 2017) and include the full continuum radiative transfer in our simulations.

Within the FEEDBACK project, clumpy KOSMA-τ results are compared to the plane-parallel results from the PDR Toolbox to test the diagnostic power of the models given the spatially and spectrally resolved data available.

Energy can be simultaneously injected in radiative (FUV photons) and kinetic (shocks) form. In the regions with evidence for shocked gas emission (for example large observed linewidths of [C II] and/or [O I]), we will compare our data to the results of dedicated modeling of irradiated shocks (Godard et al. 2019; Lee et al. 2019). These models include the effects of FUV photons on the physical conditions and chemistry of the gas. For moderate-velocity molecular shocks (up to a shock velocity of about 30 km s^{-1}), the most recent reference model was presented in Godard et al. (2019). Given the high number of input parameters, the comparison with observations is only meaningful if the number of observables (emission lines) is sufficient. In FEEDBACK regions, where this is the case and the observations in terms of linewidths justify it, our models will enable us to quantify the effects of kinetic versus radiative energy (see e.g., Figure 12 of Godard et al. 2019). A large grid of models has been run in preparation for the interpretation of FEEDBACK data, thoroughly exploring input parameters such as the pre-shock density, the shock velocity, the external radiation field, the magnetic field strength, and the PAH abundance in the observed regions. A study is in preparation to extend this model toward higher-velocity shocks (up to 60 km s^{-1}). In such shocks, additional FUV photons are generated by the shock itself (see the earlier works of Hollenbach & McKee 1989).

Summarizing, our project will investigate issues such as the relative importance of the [C II] and [O I] for gas cooling in regions of different physical conditions, the role of self-absorption in [C II] and [O I] emission and its effect on the analysis of low resolution, Galactic and extragalactic observations, and the origin of the [C II] deficit in (Ultra)Luminous IR Galaxies.

2.5. Formation of Filaments, Pillars, and Globules

Massive stars have a profound influence on the overall structure of the ISM and the proposed observations can address such key questions as: Are dense filaments formed due to the interaction of expanding, compressed shells around H II regions (see Section 2.2)? How is stellar feedback impacting an inhomogeneous molecular cloud or cloud surface? Early studies using the [C II] line (Stutzki et al. 1988; Meixner et al. 1992; Schneider et al. 1998) have revealed that FUV radiation can penetrate deep (>10 pc) into clouds with high clump to interclump density contrast, thus inducing emission from multiple PDRs along the line of sight. Simulations have also shown that geometry plays an important role. Walch et al. (2012, 2013, 2015) demonstrated that for low fractal dimensions of the cloud, the border of the H II region is dominated by shells that break up into massive high-density clumps ("shell-dominated" region) while high fractal dimensions lead to the formation of many pillars and cometary globules, containing compact dense clumps ("pillar-dominated" region). Tremblin et al. (2012b, 2012a) showed that UV radiation creates a dense shell compressed between an ionization front and a shock ahead and that density modulations in the interface produce a curved shock that collapses on itself, leading to pillar-like structures that can evolve into globules.

With the [C II] and [O I] mapping, we are able to study on a small scale (<1 pc up to a few pc) all structures in our sample that are produced under the influence of radiation such as

Table 1
FEEDBACK Sources Information

Cloud	α_{J2000}(ON) ($^h:^m:^s$) (1)	δ_{J2000}(ON) ($^\circ:':''$) (2)	α_{J2000}(OFF) ($^h:^m:^s$) (3)	δ_{J2000}(OFF) ($^\circ:':''$) (4)	d (kpc) (5)	#Tiles (6)	Area (arcmin^2) (7)	(8)
Cygnus X	20:38:20.22	42:24:18.29	20:39:48.34	42:57:39.11	1.4[a]	18	1262	PMD
M16	18:18:35.69	−13:43:30.98	18:17:17.76	−14:01:42.73	1.74[b]	12	630	PMD/CHC
M17	18:20:43.16	−16:06:14.87	18:22:01.14	−16:21:11.35	1.98[c]	13	841	PMD/CHC
NGC6334	17:20:14.07	−35:55:05.18	17:18:16.38	−35:52:28.08	1.3[d]	16	788	CHC
NGC7538	23:13:46.41	61:31:42.01	23:10:54.84	61:28:48.03	2.65[e]	4	210	PMD
RCW49	10:24:11.57	−57:46:42.50	10:27:17.42	−57:13:42.69	4.21[f]	12	788	CHC
RCW79	13:40:05.86	−61:42:36.94	13:42:08.76	−61:15:08.40	4.2[g]	9	473	CHC
RCW120	17:12:22.82	−38:26:51.61	17:10:41.01	−37:44:03.60	1.68[b]	4	210	CHC
RCW36	08:59:26.81	−43:44:14.06	09:01:31.67	−43:22:50.00	0.95[h]	4	210	CHC
W40	18:31:28.58	−02:07:35.39	18:33:08.90	−02:21:36.40	0.26[i]	12	630	PMD/CHC
W43	18:48:01.04	−01:58:22.27	18:49:30.26	−02:03:14.94	5.49[j]	12	630	PMD/CHC

Notes. (1, 2) Coordinates of the central position of the [C II] map (see Figure 1). (3, 4) Coordinates of the emission free reference position. (5) Distance in kpc. (6) Number of tiles (one tile is $7.2' \times 7.2'$) for mapping. (7) Size of mapping area in arcmin^2. (8) Visible from Palmdale (PMD) or Christchurch/New Zealand (CHC).
[a] Rygl et al. (2012).
[b] Kuhn et al. (2019).
[c] Wu et al. (2019).
[d] Chibueze et al. (2014).
[e] Moscadelli et al. (2009).
[f] Cantat-Gaudin et al. (2018).
[g] Russeil et al. (1998).
[h] Massi et al. (2019).
[i] Ortiz-León et al. (2017).
[j] Zhang et al. (2014).

pillars, globules, proplyds, and evaporating gaseous globules (EGGs). This includes the famous "Pillars of Creation" in M16 (Hester et al. 1996) as well as less known, yet equally interesting, features in other regions. The velocity resolved extended [C II] and [O I] maps are of use to investigate in more detail the dynamics of pillars and globules and allow the detection of velocity gradients, high-velocity outflowing gas and rotation. The spatial emission distributions trace the external PDR surfaces as well as internal heating sources, similar to what was found by Schneider et al. (2012b) for a globule in the Cygnus X region. The observed line intensities and ratios will be applied to the KOSMA-τ model (Röllig et al. 2006) and the PDR Toolbox for modeling the FUV-irradiated regions of the pillars and globules in order to derive the physical conditions. These can then be compared to dynamical models of pillar and globule formation (Williams et al. 2001; Mizuta et al. 2005; Gritschneder et al. 2009; Miao et al. 2009; Gritschneder et al. 2010; Tremblin et al. 2012b, 2012a).

3. Source Selection

3.1. General Considerations

We have selected a sample of sources that were included in the Spitzer/GLIMPSE and Herschel HOBYS (Motte et al. 2010), Gould Belt (André et al. 2010) and Hi-Gal (Molinari et al. 2010) Legacy/Key Programs. Northern sources are observed with flights originating from the Armstrong Flight Research Center in Palmdale, California, and southern sources with flights from Christchurch, New Zealand. Tables 1 and 2 and Figure 1 give an overview of the sample. In the selection we ensured that a wide range in star formation activity is covered, from regions dominated by single O stars, by small groups of O stars, by compact clusters, by super star clusters, and by mini starbursts.[17] Another consideration was to include regions that are probably at different stages of their evolution (see individual source descriptions below). Morphology was an important criterion (see Section 2.1) and we incorporated H II regions that are (almost) perfect spherical bubbles, multi-bubbles or broken bubbles, bipolar structures, all with or without pillars and globules. Regions with more dispersed star formation activity and clouds with many filaments and massive ridges were also considered. Furthermore, the selected sources include regions dominated by the thermal expansion of ionized gas (Spitzer-type expansion), by stellar wind driven flows, by radiation pressure, by the concerted interaction of multiple expanding H II regions, by the presence of nearby rich OB associations, and by the action of converging flows associated with the large scale spiral arm structure of the Milky Way. This allows us to study feedback on a wide range of

[17] We follow the definition by Motte et al. (2003) that a Galactic mini starburst region is a cloud with a star formation efficiency as high as 25%.

Table 2
FEEDBACK Sources Physical Properties

Cloud	⟨FUV⟩ G_0 (1)	FUV-range G_0 (2)	SpT (3)	v_{lsr} (km s^{-1}) (4)	Mass (10^3 $M_\odot$) (5)	Cloud Geometry (6)	H II Region Geometry (7)
Cygnus X	290	200-7.6 × 10^4	∼50 O, 3 WR	−3	200	ridge/filaments	bubbles and compact
M16	300	270–8.7 × 10^3	1 O4, ∼10 late O	25	87	radiation sculpted interfaces	irregular
M17	1295	300–4.6 × 10^4	2 O4, ∼10 late O	22	483	clumpy	irregular
NGC6334	580	500–8.9 × 10^4	5 O5–8, 8 B	8	239	ridge/filaments	many bubbles
NGC7538	904	10^3–3.9 × 10^5	1 O3	−55	130	clumpy, ring	evolved bubble
RCW49	555	200–5 × 10^3	2 WR, 12 early O	0	170^+	fragmented	irregular/evolved bubble
RCW79	140	35–5 × 10^3	2 O4, ∼10 late O	−50	146	fragmented	evolved bubble
RCW120	375	100–1.5 × 10^4	1 O8	−10	20	ring/shell	bubble
RCW36	413	300–1.5 × 10^4	1 O8, B-cluster	5	58	ridge	bipolar
W40	237	150–8.2 × 10^3	1 O, 2 B	5	26	clumps/filaments	bipolar
W43	741	700–5.9 × 10^4	OB, WR cluster	100	6000	ridge/filaments	bubbles and compact

Note. (1) Spatially averaged FUV field in Habing units, determined from Herschel FIR-fluxes at 70 and 160 μm (Schneider et al. 2016). (2) FUV range in Habing units within the [C II] mapping area, determined from Herschel FIR-fluxes at 70 and 160 μm. (3) Spectral type(s) and number of dominating star(s). (4) Approximate local-standard-of-rest velocity of the source. (5) Approximate mass of the associated molecular cloud derived from Herschel dust column density maps (N. Schneider et al. 2020, in preparation).$^+$Mass determined from CO 1 → 0 data (Furukawa et al. 2009). (6) Type/geometry of the molecular cloud region and interface. (7) Type/geometry of the H II region.

scales both in size (from sub-pc to tens of pc) and energy (energy of a single O star to that of clusters of stars containing tens to hundreds of OB stars).

The sample comprises well-known sources dominated by these different dynamical processes (thermal, wind, radiation pressure) and covers the parameter space of star formation activities and evolutionary stages.

3.2. Complementary Data Sets

Much ancillary data is available for all regions as they have been studied in depth in a variety of Herschel and Spitzer programs. These surveys provide detailed spectral energy distributions, luminosities, dust temperatures, and column densities at spatial scales that are comparable to those that are obtained by the upGREAT mapping of [C II] and [O I]. Source catalogs from various instruments are available for a census of ongoing star formation activity (pre- or protostellar cores, protostars).

We use existing molecular line data (mostly CO) from publically available large surveys (e.g., the FUGIN project from the Nobeyama telescope for M16, M17, and Aquila, and dedicated molecular line and atomic carbon observations using the APEX telescope (Güsten et al. 2006). We already obtained ^{12}CO and ^{13}CO 3 → 2 maps for some sources, performed recently with the new LAsMA array on APEX (RCW120 was among these sources and spectra are shown in Section 5.2). LAsMA is a 7-pixel single polarization heterodyne array that allows simultaneous observations of the two isotopomers in the upper (^{12}CO) and lower (^{13}CO) sideband of the receiver, respectively. The array is arranged in a hexagonal configuration around a central pixel with a spacing of about two beam widths (the beamwidth is 18.″2 at 345.8 GHz) between the pixels. It uses a K mirror as de-rotator. The backends are advanced Fast Fourier Transform Spectrometers (Klein et al. 2012) with a bandwidth of 2 × 4 GHz and a native spectral resolution of 61 kHz. APEX will also be used for observations of the atomic carbon line at 490 GHz and the CO 6 → 5 line.

The [C I] line at 490 GHz was already mapped with the 4GREAT instrument on SOFIA for NGC7538 and Cygnus (in parallel, 3 high-J CO lines were observed). More observations of [C I] and CO lines and of the [O I] 145 μm line for the FEEDBACK sources are planned.

We also recently finished a program to observe radio-recombination lines of hydrogen, helium, and carbon in M17, M16, W40, Cygnus X, and NGC7538 at the Green Bank Telescope.

3.3. Details of Individual Sources

Information on the individual sources (and of the program in general) is found on the webpages of the FEEDBACK program: https://feedback.astro.umd.edu and https://astro.uni-koeln.de/18620.html. We here give a short summary for each source (see also Tables 1 and 2).

Cygnus X

The Cygnus X region (Reipurth & Schneider 2008) is one of the richest star formation sites in the Galaxy, mainly excited by the Cygnus OB2 association that contains well over 100 OB stars (Comerón et al. 2002; Wright et al. 2015). Most of the molecular clouds are located at a distance of 1.4 kpc (Rygl et al. 2012), the total molecular gas mass is a few 10^6 $M_\odot$ with an average density of ∼60 cm^{-3} (Schneider et al. 2006) and densities >10^5 cm^{-3} in clumps and cores associated with

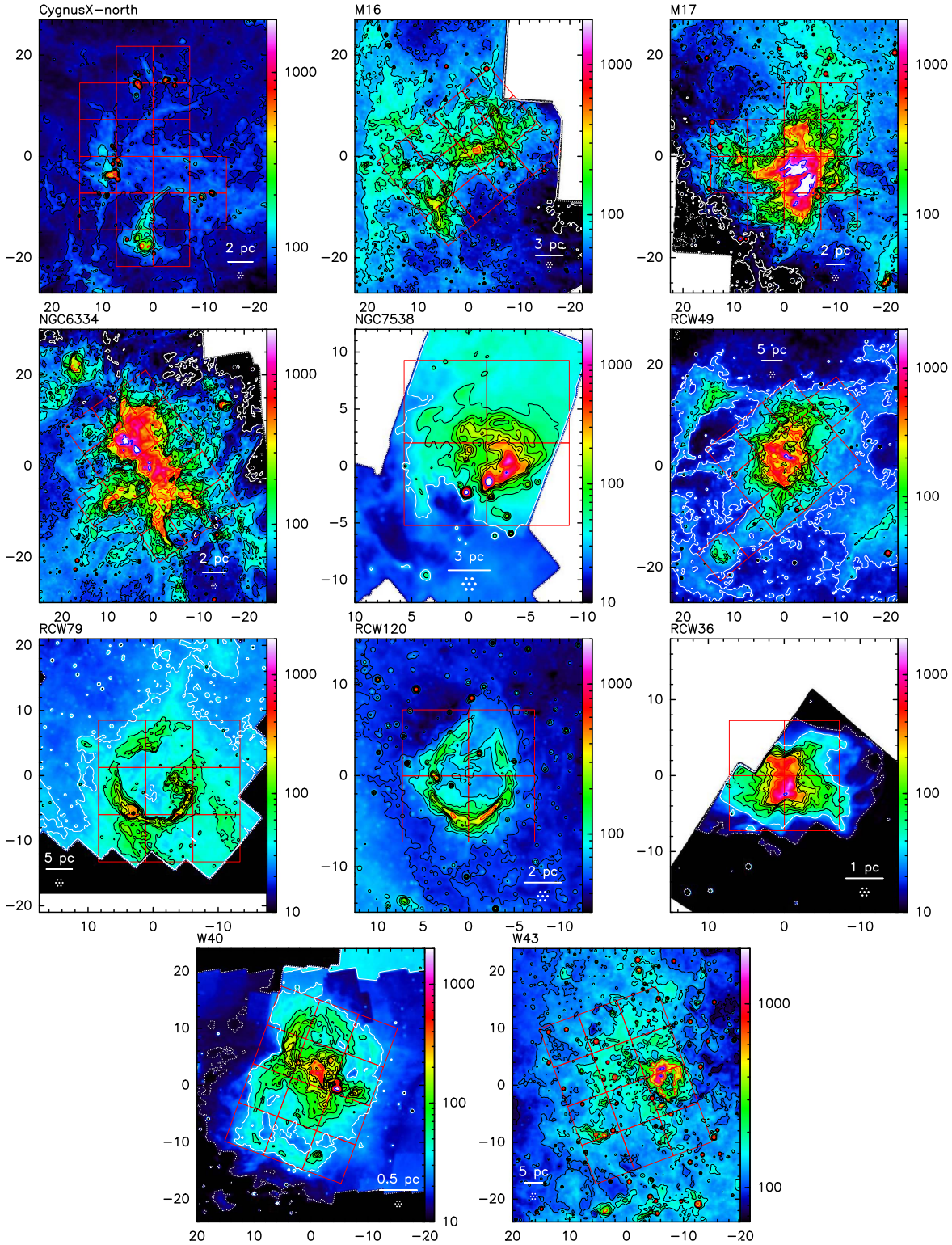

Figure 1. IRAC 8 μm maps of the FEEDBACK sources in color (in MJy/sr), convolved to the upGREAT beam of 14.″1). Contours are predicted [C II] integrated line intensity based upon the [C II]–8 μm relation derived for L1630, Orion, and 30 Dor (Pabst et al. 2017, 2019). Contour levels are: white dashed (50 K km s^{-1}), white (100 K km s^{-1}), black (150, (50), 400 K km s^{-1}), red (500 K km s^{-1}), blue (1000 K km s^{-1}). The LFA/upGREAT 7 beam pattern is plotted in a corner in each box. The overlaid red boxes represent the tiles that cover the [C II] mapping area. The images show RA, Dec offsets in arcmin with respect to the (0, 0) position given in Table 1. (A color version of this figure is available in the online journal.)

ongoing star formation. The northern part of Cygnus X contains the prominent DR21 and W75N regions that are located within dense filamentary structures, called "ridges" (Schneider et al. 2010; Hennemann et al. 2012). The average UV-field is high ($\sim$300 $G_\circ$) and reaches peak values up to $\sim 10^5$ $G_\circ$ in PDRs close to Cyg OB2 (Schneider et al. 2016). The interaction of UV radiation with the molecular clouds created a wealth of structures such as pillars, globules, EGGs, and proplyd-like features (proplyds are evaporating circumstellar disks, but the sources found by Wright et al. (2012) in the immediate environment of the Cyg OB2 association are much larger than typical proplyds). Based on this classification using Herschel data, Schneider et al. (2016) proposed an evolutionary scheme in which pillars can evolve into globules, which in turn then evolve into EGGs, condensations and proplyd-like objects.

We study the northern Cygnus X region because it shows many sequential stages of star formation and—as a large complex—is a key to understanding the role that massive star complexes play in external galaxies. The Cygnus X North region is exposed to a high overall radiation field, mostly arising from Cyg OB2, but also from many local H II regions. For FEEDBACK, we focus on mapping the DR21 ridge and the "Diamond Ring" (Marston et al. 2004), an H II region southwest of DR21.

M16

The Eagle Nebula (M16) is a young (1–3 $\times$ 10^6 yr), active high-mass SF region in Serpens. Guarcello et al. (2010) proposed that the stars in the northwest part of the H II region are younger than the stars in the southeast part and that a 200 pc shell triggered the formation of both M16 and M17 3 Myr ago on much larger scales. Responsible for heating and ionizing the Nebula is the young open star cluster NGC6611, containing four early-type O stars, leading to a high average UV-field of $\sim$300 $G_\circ$. The transition between H II region and dense, cold gas is rather sharp with many UV-illuminated features. In particular Hubble Space Telescope imaging of the "Pillars of Creation" has made M16 iconic.

M16 is well suited to study the mechanical (stellar winds) and radiative energy (UV field) incident on the molecular cloud complex, shaping the gas into pillars and other features. In contrast to the Cygnus X region, M16 does not show free-floating objects such as globules or proplyds. We thus focus on pillar structures that are a common morphological phenomenon, appearing on the boundaries of many evolved H II regions (Dent et al. 2009; Pound et al. 2003; Xu et al. 2019). Herschel studies (Hill et al. 2012b) showed that the cluster affects the temperature within the molecular cloud, modifying the initial conditions for collapse and affecting the evolutionary criteria of protostars, for example increasing the bolometric temperature and the $L_{\rm submm}/L_{\rm bol}$ ratio. The brightest area of M16 is smaller than other massive SF regions and can be fully covered in the [C II] line, including the Pillars, the Spire, and the Arch.

M17

M17 is located at a distance of 1.98 kpc (Wu et al. 2019) and associated with the highly obscured ($A_V > 10$) cluster NGC6618 with more than 100 OB stars. The edge-on geometry allows to study feedback of the rich cluster with the molecular cloud all along the interface and into the highly clumpy molecular cloud. The total mass of the complex (from CO observations) is 2 $\times$ 10^4 $M_\odot$ and can be split into M17 North (M17–N) and M17 Southwest (M17–SW). For M17–N (M17–SW), the density ranges between 10^4–10^5 cm^{-3} (10^6 cm^{-3}) (Stutzki & Güsten 1990; Meixner et al. 1992; Wilson et al. 2003). M17–SW has been studied extensively in many different tracers and frequencies. A recent SOFIA [^{13}C II] study reveals unexpectedly large columns of warm and cold [C II](Guevara et al. 2020).

NGC6334

NGC 6334 is a very active star-forming region (see e.g., Persi & Tapia 2008) with a remarkably large number of H II regions spread across the complex (7 compact and optical H II regions per square degree) at a distance of 1.3 kpc (Chibueze et al. 2014). Most of the H II regions have a bubble-like morphology in the IR, FIR and optical, but there are also examples of an expanding wind shell-like H II region (GUM61) or champagne flow (GUM64b), see e.g., Russeil et al. (2016). The associated molecular cloud consists of a $\sim$10 pc long, dense filament that is associated with strong extinction and is embedded in a larger $\sim$50 pc-long, less dense filamentary cloud (Zernickel et al. 2013; Russeil et al. 2016). A number of active star formation sites exist within the dense filament (Brogan et al. 2016; Juarez et al. 2017; Tigé et al. 2017; Sadaghiani et al. 2020) with compact H II regions detectable at radio wavelengths such as NGC 6334-I and NGC 6334-E being driven by a rich embedded cluster of B-type stars. The average UV-field ($\sim$580 G_0) is above the median within the selected sample.

The gas dynamics in NGC 6334 are dominated by the large number of H II regions (Russeil et al. 2016), in particular for the dense 10 pc long filament. This one is also undergoing longitudinal collapse (Zernickel et al. 2013) and is also likely compressed by the expansion of the two large H II region bubbles to the north and south (Russeil et al. 2013). Structure analysis based on the Δ-variance method applied to the *Herschel* H_2 column density maps identified characteristic scales that can be caused by the injection of energy due to expanding H II regions (Russeil et al. 2013).

NGC7538

NGC7538 is a small H II region, which is part of the Cas OB2 complex at a distance of 2.65 kpc (Moscadelli et al. 2009). It is illuminated by a group of O stars of spectral type O6-O9. The dominant ionizing star of NGC7538 has been classified as

an O3 or an O5 star (Ohja et al. 2004; Puga et al. 2010), the radio data is consistent with an O5 star (Luisi et al. 2016).

NGC7538 is expanding into a massive star-forming cloud south and southeast of the H II region and has most likely triggered star formation in the cloud. Especially the extremely young O star IRS1, which is located at the boundary between the expanding H II and the molecular cloud, is still heavily accreting and surrounded by a cluster of mm-continuum sources, which are probably all young pre-main-sequence sources (Frau et al. 2014).

RCW49

RCW49 is one of the most luminous and massive H II regions of the southern Galaxy. From recent GAIA observations, its distance is determined to be 4.21 kpc (Cantat-Gaudin et al. 2018), slightly further away than the 4.16 kpc determined by Vargas-Alvarez et al. (2013) from spectroscopy. It hosts the Westerlund 2 (Wd2) cluster, comprising a dozen of OB stars and 30 OB star candidates around it (Tsujimoto et al. 2007; Rauw et al. 2011; Zeidler et al. 2015). A binary Wolf–Rayet star (WR20a), perhaps the most massive binary in the Galaxy, is associated with the cluster and its presence indicates that the cluster is a few 10^6 yr old. Beyond the cluster core are at least two very massive stars, which include an O4 or O5 star and another Wolf–Rayet star (WR20b). More than 3000 X-Ray point sources were found centered on Wd2 and toward its west lies a pulsar wind nebula surrounded by diffuse X-Ray emission (Townsley et al. 2019). Stellar winds from Wd2 and from the surrounding stars play an important role in the star formation occurring in RCW49.

The velocity dispersion of the associated molecular gas suggests that collision between two CO molecular clouds in the velocity ranges -11 to 9 km s^{-1} and 11 to 21 km s^{-1} also contributed to the formation of the stellar cluster Furukawa et al. (2009). Whiteoak & Uchida (1997) reported the presence of two wind driven shells at the center of RCW49. We assume that both the stellar winds and cloud-cloud collision are responsible for the morphological evolution of the bubbles associated with RCW49.

RCW79

The RCW79 bubble is ionized by a cluster of a dozen O stars, the two most massive of which have a spectral type O4–6V/III (Martins et al. 2010). The ionizing luminosity of the ionizing stars was estimated to be 10^3 times higher than the mechanical luminosity of their stellar winds, indicating a radiation driven H II region. RCW79 is spatially encompassed by an almost complete dust ring, with a diameter of 12′, corresponding to ∼12 pc at a distance of 4.2 kpc (Russeil et al. 1998). Liu et al. (2017) suggested that triggered star formation might occur around this bubble. Based on Herschel data for RCW79 (Liu et al. 2017), more than 50 compact sources (Class 0 and I) were found in the ionization-compressed layer of cold and dense gas from which 12 are candidate massive dense cores that may form high-mass stars. The core formation efficiency (CFE) shows an increase with increasing density, suggesting that the denser the condensation, the higher the fraction of its mass transformation into dense cores.

RCW120

This source is a well-studied, bubble-shaped H II region of ∼4.5 pc diameter, excited by an O8V star, CD −38°11636, at a distance of 1.68 kpc (Kuhn et al. 2019). RCW 120 has become sort of a poster-child (Zavagno et al. 2010; Anderson et al. 2015) of the myriad of bubbles discovered by the GLIMPSE survey. The H II region is surrounded by a dense shell of gas and dust, observed in dust (Deharveng et al. 2009; Zavagno et al. 2010; Anderson et al. 2015; Figueira et al. 2017; Zavagno et al. 2020) and molecular lines (Torii et al. 2015; Kirsanova et al. 2019). Remarkable is an arc of emission visible at 24 μm south of the ionizing star because it may represent the upstream boundary between the wind bubble and photoionized gas (Mackey et al. 2015). There is an ongoing discussion whether the ring-shape appearance of RCW120 is due to an expanding H II region (Deharveng et al. 2009; Zavagno et al. 2010) or a cloud-cloud collision (Torii et al. 2015). Using Herschel observations Anderson et al. (2012) found that 20% of the total FIR emission of bubble H II regions comes from the direction of bubble "interiors," the locations inside the PDRs, which suggests a three-dimensional morphology.

RCW36

RCW36 is among the closest H II regions to the Sun, at a distance of 950 pc (Massi et al. 2019) within the Vela C molecular cloud. The H II region has a bipolar shape and is surrounded by molecular gas with a dust lane that crosses the bipolar cavity. The embedded cluster (∼350 stars) with the most massive star being a type O8 or O9 is located within the cavity (Baba et al. 2004). The cluster extends over a radius of 0.5 pc, with a stellar surface number density of 3000 stars pc^{-2} within the central 0.1 pc. Herschel studies suggest that the bipolar morphology has evolved from its filamentary beginnings under the impact of ionization (Minier et al. 2013).

The bipolar H II region RCW36 is also an example of a region for the interplay between ionization and structures (bright rims and pillars) around an H II region. Comparing the dynamics of [C II] and CO emission (Fissel et al. 2019) will address the question whether filamentary structures can be the location of very dynamical phenomena inducing the formation of dense clumps at the edge of H II regions. Moreover the [C II] mapping of this region will lead to a better understanding of the formation of bipolar nebulae as a consequence of the expansion of an H II region into a molecular ridge or an interstellar filament.

W40

The W40 complex is a nearby (260 pc, Massi et al. 2019) site of high-mass star formation associated with a cold molecular cloud ($\sim 10^4\,M_\odot$) and includes a blistered H II region powered by an OB association and two interconnected cavities, forming an hour-glass shape on large scales (a few pc). The main cluster

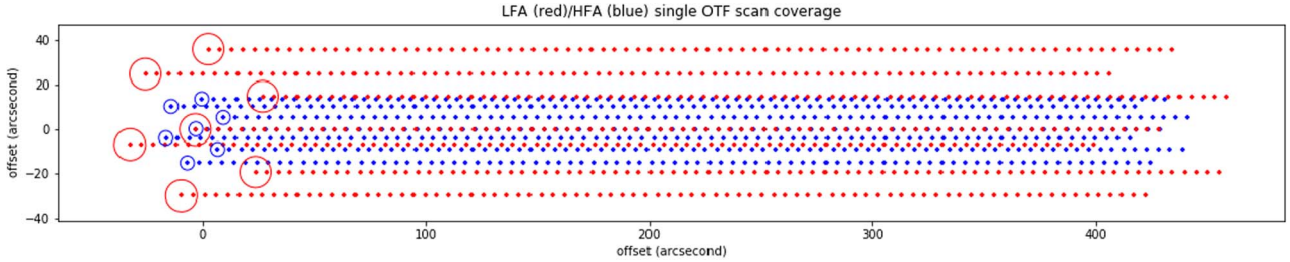

Figure 2. LFA (red) and HFA (blue) footprints (diameter of the circles correspond to the FWHM of the beams) of the 7 pixel arrays (the LFA has 2 × 7 pixels, one in horizontal and one in vertical polarization) as they appear on the sky for one scan. The dotted lines show the scan direction, each dot represents one dump. The array is rotated by 19° relative to the scan direction. The LFA array size is 72.″6 (pixel spacing of 31.8″) and the HFA array size is 27.″2 (pixel spacing of 13.6″). (A color version of this figure is available in the online journal.)

is located just northwest of the narrow waist where the two cavities are joined. The bright-rimmed clouds at the cavity walls show clearly that dense clumps and pillars are illuminated from inside by the cluster. The OB association is comprised of IRS/OS1a (O9.5), IRS/OS2b (B4) and IRS/OS3a (B3) and an associated stellar cluster of pre-main-sequence stars (Shuping et al. 2012).

The W40 molecular cloud/H II region is one of the few nearby regions with active high mass star formation, hosting an embedded cluster (Könyves et al. 2015). The [C II] mapping will focus on the bipolar cavity walls illuminated by the cluster to study the feedback of the OB cluster on the surrounding molecular cloud.

W43

W43 is one of the most active star-forming regions in the Galaxy. Its position in the Galactic plane and its radial velocity place it at the junction point of the Galactic long bar and the Scutum spiral arm at 5.5 kpc distance to the Sun. It contains two of the most massive cloud groups of the first Galactic quadrant (W43 Main and South) with a total mass of $\sim 6 \times 10^6\ M_\odot$ (Carlhoff et al. 2013; Motte et al. 2014). W43 Main is heated by a cluster of Wolf–Rayet and OB stars ($\sim 3.5 \times 10^6\ L_\odot$) and is considered to be a Galactic mini starburst region (Motte et al. 2003; Bally et al. 2010) since it is undergoing a remarkably efficient episode of high-mass star formation (∼15 high-mass protoclusters and a star formation efficiency (SFE) of $\sim 0.1\ M_\odot\ \mathrm{yr}^{-1}$).

The formation of the associated ionizing cluster was likely supported by the expansion of an older H II region to the south that triggered the formation and gravitational collapse of the GMC that evolved into W43. Subsequently, UV radiation from the central O+WR cluster compressed the parent cloud toward both low- and high Galactic longitudes, triggering the formation of additional massive stars. Its mini starburst activity is continuously fueled by converging flows, owing to its position at the junction point of the Scutum-Centaurus (or Scutum-Crux) Galactic arm and the Bar (Beuther et al. 2012; Motte et al. 2014).

Its position in the Galaxy makes W43 a very interesting object for studying the formation of molecular clouds and the feedback in a dynamically extreme environment. Despite its distance, it is possible to analyze the details of this cloud, due to its large spatial scale of 150 pc and the large amount of gas at high density.

4. Observation Strategy and Planning

4.1. Definition of Mapping Area

We have estimated the [C II] 158 μm surface brightness from 8 μm PAH emission maps (convolved to the upGREAT beam) because the latter are signposts of bright PDR gas and [C II] and 8 μm brightness are very well correlated with each other (Pabst et al. 2017, 2019; Anderson et al. 2019). The map extent was defined by a certain expected level of [C II] line integrated intensity (varying between 100 and 250 $\mathrm{K\,km\,s^{-1}}$, depending on source) and compared to maps of the far-UV field, derived from 70 and 160 μm Herschel/PACS flux maps (see procedure described in Schneider et al. 2016). Typically, the mapping area starts above 100 $G_\circ$. Figure 1 shows the area to be covered by the tiles of the [C II] mapping overlaid on IRAC 8 μm maps in color. The emission free reference positions for each map are listed in Table 1.

4.2. upGREAT

All sources are mapped with the dual-frequency heterodyne array receiver upGREAT[18] heterodyne receiver (Risacher et al. 2018) with the [C II] 158 μm (1.9 THz) tuned in the LFA 2 × 7 pixel array and the [O I] 63 μm (4.7 THz) line tuned in the HFA 7 pixel array. The LFA has an array size of 72.″6, and a pixel spacing of 31.″8 while the HFA has an array size of 27.″2 and a pixel spacing of 13.″6 (see Figure 2 for a footprint of the arrays on the sky during one scan). The half-power beam widths are 14.″1) (1.9 THz) and 6.″3 (4.7 THz), determined by the instrument and telescope optics, and confirmed by observations

[18] German Receiver for Astronomy at Terahertz. (up)GREAT is a development by the MPI für Radioastronomie and the KOSMA/Universität zu Köln, in cooperation with the DLR Institut für optische Sensorsysteme.

of planets. The receiver noise temperatures are 2000 K for the LFA and 2500 K for the HFA (see Table 1 in Risacher et al. 2018). The backends for both channels are Fast Fourier Transform Spectrometer (FFTS) with 4 GHz instantaneous bandwidth (Klein et al. 2012). The frequency resolution of the raw [C II] and [O I] data is hardware selected to 0.244 MHz, giving a velocity resolution of 0.04 km s^{-1} and 0.015 km s^{-1}, respectively. The data cubes provided to the SOFIA science center and used by the FEEDBACK consortium have a resampled velocity resolution of 0.2 km s^{-1}.

Procedures to determine the instrument alignment and telescope efficiencies, antenna temperature and atmospheric transmission calibration, as well as the spectrometers used, are described in Risacher et al. (2016, 2018) and Guan et al. (2012). For each flight series, the main-beam efficiencies ($\eta_{\rm mb}$) for each pixel for the LFA and HFA channels are determined, typical values are $\eta_{\rm mb} = 0.65$ (0.69) for [C II] ([O I]). The forward efficiency is $\eta_f = 0.97$.

The telluric [O I] line, originating from the mesosphere, can contribute as a narrow feature in the observed band. The half-intensity width of this non-Gaussian line is typically 1 km s^{-1}. We try to schedule each source at an observing time of the year when the mesospheric line does not appear at the velocity of the bulk emission. However, because of flight planning constraints and because the [C II] line is the main science driver, this is not always possible. We will endeavor to maximize the scientific return around the atmospheric line, but the line can be rather opaque at the line center. We will need to fine tune the atmospheric model layering of the mesophere to determine the correct transmission on the wings of the atmospheric [O I] line profile. Atomic oxygen is now included in the latest version of the "am" atmospheric code (Paine 2019) used to calibrate the upGREAT data. The large FEEDBACK data set should give us ample data to constrain the distribution of atomic oxygen in the atmosphere (H.-W. Hübers et al. 2020, in preparation).

We will also consider to apply a correction for the absorption following the procedure described in Leurini et al. (2015) and Schneider et al. (2018), assuming that the profile can be characterized by a Gaussian. In summary, for the opacity correction, the absorption strength was adjusted in a way to achieve an adequate interpolation between adjacent unaffected spectral channels.

The thus corrected [O I] data will be delivered later as a Level 4 data product.

4.3. Mapping Scheme

Mapping was performed in an optimized array-on-the-fly mapping mode. Each region was split into multiple square "tiles" with 435.″6 on one side and each square was covered 4 times. The OTF scan speed was selected to attain Nyquist sampling of the LFA beam (dump every 5.2″) while the HFA is undersampled. The total time for one OTF line is then 25.2 s. This is, together with the OFF observation, within the measured Allan variance stability time of the system. The Allan variance of the LFA system is of the order of 80–100 s under stable ambient temperature conditions but can decrease to 30–35 s if there are temperature instabilities or drifts onboard the SOFIA aircraft (Risacher et al. 2018). The first two coverages are done once horizontally and vertically with the array rotated 19° against the scan direction, so that scans by 7 pixels are equally spaced. The second two coverages are then shifted by 36″ in both directions to achieve the best possible coverage for the [O I] line in the LFA array mapping mode (Figure 3). Each tile takes ≈50 minutes to complete. This mode of operation is a slightly modified version of the mode used in the [C II] survey of the Orion molecular cloud (Pabst et al. 2019) and R. D. Higgins et al. 2020, in preparation, where the second coverage was performed with rotating the hexagonal array by 60° instead of shifting the mapping positions. The mode used in the FEEDBACK project achieves a higher degree of redundancy as each pixel maps a different strip of sky during each scan. Most importantly, though, this mode returns a better, though not fully sampled, coverage of [O I]. The only disadvantage is that the [C II] maps may show edge effects since some LFA coverage is sacrificed toward 2 sides of the map edges. However, there is still a uniform noise coverage for the LFA. At the beginning of each flight leg for the project, a short calibration observation of a single point in each source is performed to monitor the line intensity if the observations extend over several flights.

4.4. Data Reduction

Spectra are presented on a main beam brightness temperature scale $T_{\rm mb}$. Recommended main beam coupling efficiencies are presented in the notes "Project Overview" in the SOFIA science archive. All pixels have been calibrated individually and there are slight efficiency variations depending on the Cycle when the sources were observed. For the sources observed in Cycle 7 and 8, the main-beam effciencies are typically 0.65 for [C II] and 0.69 for [O I]. The calibrated [C II] and [O I] spectra were further reduced and analyzed with the GILDAS[19] software. From the spectra, a 3rd order baseline was removed and the spectra were then gridded with $1/\sigma^2$ weighting (average baseline noise).

4.5. RCW120 Data

The example data we show in this paper (Figures 4 and 5) were obtained during one flight from Christchurch, New Zealand on 10th of June 2019 (flight F579). Three out of the four planned tiles were observed in the mapping scheme described in Section 4.3 (the last tile was not completed so that

[19] GILDAS is developed and maintained by IRAM.

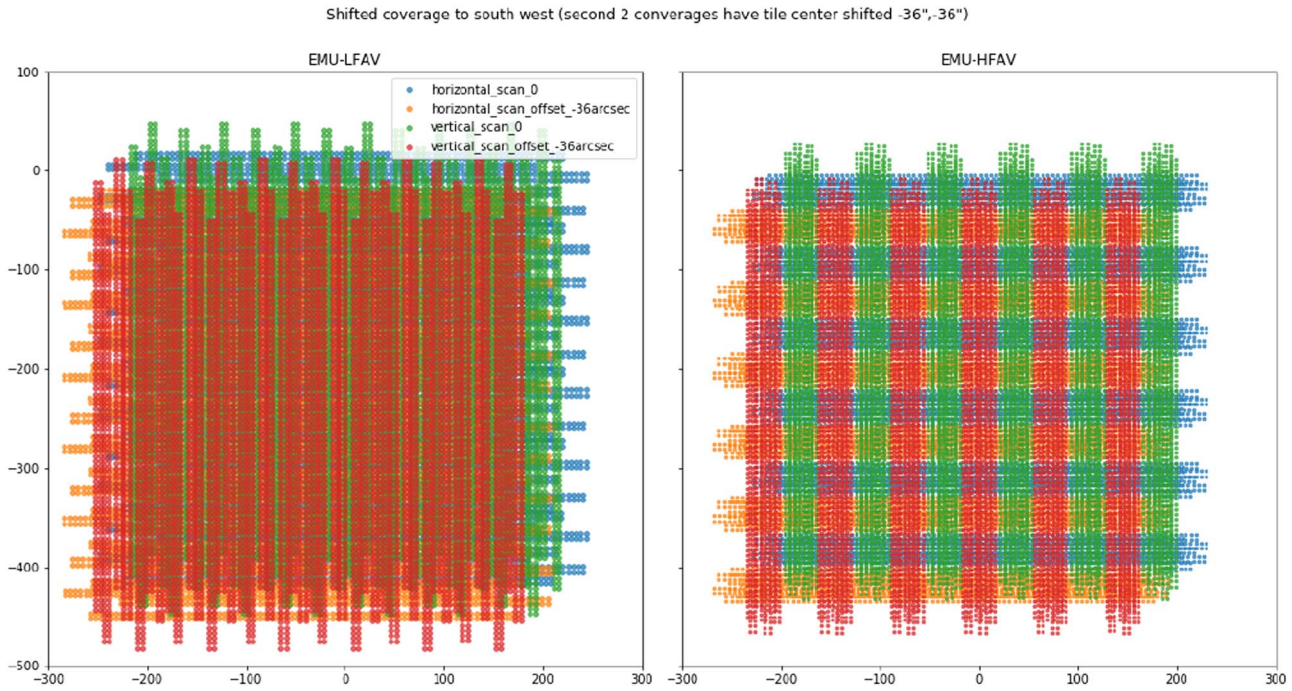

Figure 3. Optimized array mapping for [C II] and [O I] observations. The left panel shows the 4 coverages for the LFA channel ([C II] line) and the right panel the resulting coverage for the HFA channel ([O I] line). The observations start with a horizontal scan (blue), followed by a vertical scan (green). Then, the tile center is shifted by $-36''$, $-36''$ and another horizontal and vertical scan (orange and red, respectively) are performed. The shift of the second coverage is chosen in order to fill the gap in the HFA map.
(A color version of this figure is available in the online journal.)

72% of the map is finished). The data were reduced as outlined in Section 4.4. The [O I] mesospheric line at $\sim$8 km s^{-1} was not much affecting the astronomical [O I] line at around -8 km s^{-1}. We here show preliminary data that were obtained by removing a third order baseline, and excluding the velocity range of the [O I] telluric line.

5. First Results

5.1. Current State of Observations

As of April 2020, observations for 32% of the 96h of the observing time of the FEEDBACK program have been performed. The state of observations is constantly updated and is shown on the Cologne FEEDBACK webpage. The most advanced map is that of RCW120 (Section 5.2) with 72% completed. The H II bubble RCW49 is 65% complete, and RCW36 in Vela 51%. For all other sources, the completeness is less than 20%.

5.2. [C II] and [O I] Observations of RCW120

We selected the RCW120 region as an example for the mapping capabilities of upGREAT on SOFIA because these observations are the most progressed. The maps and spectra shown in this subsection are preliminary and intended to give a first impression of the nature and the quality of the data that the FEEDBACK program will deliver. It is not our objective here to discuss in more detail the science, which will be done in M. Luisi et al. (2020, in preparation) and other upcoming publications. Figure 4 shows the line integrated [C II] map, smoothed to $15''$ angular resolution (the [C II] beam is $14\farcs1$)) and on a $3\farcs5$ grid. The velocity range for integration was -30 to $+10$ km s^{-1} which covers all relevant velocity ranges of [C II] emission. The overall structure is shell-like with two emission peaks in the southwest (up to $\sim$300 K km s^{-1}) and southeast (up to $\sim$200 K km s^{-1}), and more diffuse emission from the bubble center. These two peaks correspond to condensations 1 and 2 labeled by Zavagno et al. (2010).

Figure 5 displays an averaged [C II] spectrum over the southwestern clump, indicated in Figure 4 as a dashed polygon, together with spectra of [O I] 63 μm, and ^{12}CO 3 $\rightarrow$ 2 and ^{13}CO 3 $\rightarrow$ 2 data from APEX, averaged over the same area. Note that the [O I] line shows some baseline structures because we conservatively only removed a baseline order 3 for this preliminary data reduction. The [C II] spectrum shows a prominent blue tail, reaching up to -30 km s^{-1} which is not apparent in the other lines. All spectra have a double-peak structure which is most prominent for the ^{12}CO 3 $\rightarrow$ 2 and the [O I] line with a deep dip at ~-8 km s^{-1}. Because the [C II] line and the ^{13}CO 3 $\rightarrow$ 2 line (which is commonly considered to be optically thin) also show a dip at that velocity—though

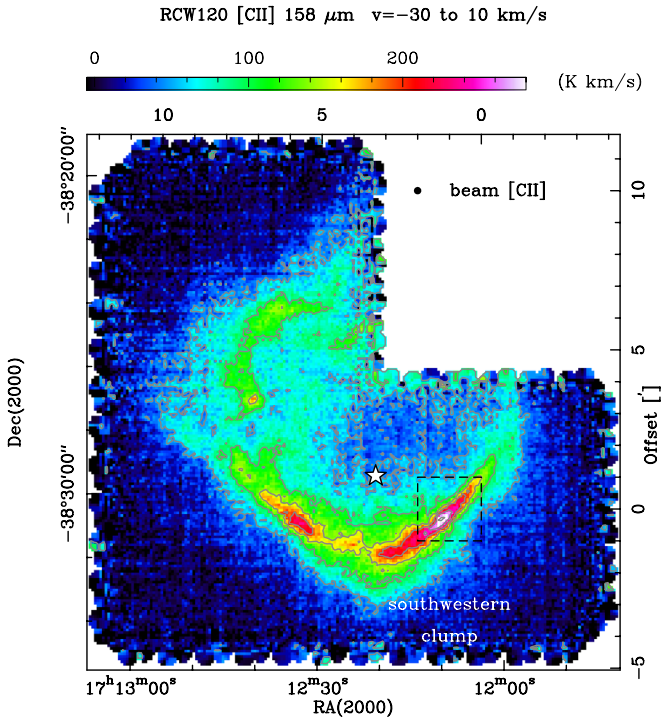

Figure 4. SOFIA/upGREAT map of line integrated [C II] emission in RCW120 smoothed to an angular resolution of 15″ and with a gridding of 3.5″. The star marks the position of the exciting O8V star CD38-11636. The dashed rectangles indicate the area used for averaging the spectra presented in Figure 5.

(A color version of this figure is available in the online journal.)

not as deep as the one for [O I] and ^{12}CO—the interpretation of this profile can be twofold. Either all 4 lines are affected by self-absorption, or there are individual velocity components. Self-absorption is the most likely explanation, though it requires a complex layering of various gas components at different densities and temperatures along the line of sight because the excitation conditions for all lines are distinct (Section 1). While the [C II] line is thermally excited at temperatures around 100 K and densities of a few 10^3 cm^{-3}, the CO lines require higher densities (a few 10^4 cm^{-3}), and the [O I] line has the highest critical density of 10^5 cm^{-3} and necessitates temperatures >200 K. A temperature gradient clearly exists, with higher values in the PDR facing the inside of the shell. Herschel dust observations (Anderson et al. 2010) show temperatures >30 K in the interior of RCW120 (with a hot dust component around 100 K), ∼20 K in the PDR, and ∼10 K in the cool molecular shell. In addition, YSOs in different evolutionary phases from Class 0 to Class I were detected in the southwestern clump (Figueira et al. 2017) and could contribute as internal heating sources. Clumpiness of the shell would lead to higher density, cool clumps embedded in a lower density, warm interclump medium. Self-absorption in the observed CO lines requires cool, low-density gas.

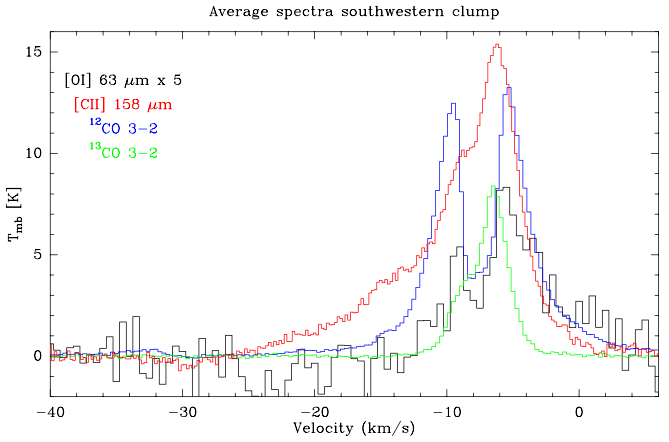

Figure 5. Positionally averaged spectra of [C II] (red), [O I] (black), ^{12}CO 3 → 2 (blue), and ^{13}CO 3 → 2 (green). Figure 4 shows the area of integration in the southeastern clump. Note that the [O I] line temperature is multiplied by 5 for better visibility. The [O I] and ^{12}CO lines show a strong dip at −8 km s^{-1} which is also visible—though less prominent—for the [C II] and ^{13}CO 3 → 2 lines.

(A color version of this figure is available in the online journal.)

Kirsanova et al. (2019) fitted their ^{13}CO 3 → 2 and 2 → 1 observations with a foreground cloud with a density of about 50 cm^{-3} and a temperature <60 K. This gas component would also lead to self-absorption in the [C II] line. A more detailed investigation is out of the scope of this paper, but will be done in a furthcoming study (S. Kabanovic et al. 2020, in preparation). We will then also use observations of the [^{13}C II] line to determine the optical depth of the [^{12}C II] line and employ models of several emission and absorption layers, similar as it was done in Guevara et al. (2020) for M17.

6. Data Products

For each source, Level 3 data products with calibrated [C II] maps are delivered to the SOFIA Science Center by the GREAT team. The data are accessible via the NASA/IPAC InfraRed Science Archive[20] No account is required to access the archive, and the FEEDBACK data are available to the public upon their ingestion. FEEDBACK data can be accessed at IRSA by searching by source (under "Spatial Constraints") or by Plan ID 07_0077 (under "Proposal Constraints"). The Level 3 data in the archive were produced by removing a third order spectral baseline, calibration to T_{mb} temperature scale, resampling to 0.2 km s^{-1} spectral resolution, and filtering using the ratio of (baseline rms)/(expected radiometer noise) <1.40. Level 4 data, for which further issues such as, e.g., standing waves or the mesopheric [O I] line are addressed, will be delivered later.

[20] https://irsa.ipac.caltech.edu/applications/sofia.

7. Conclusions

We presented the goals and first promising results of the SOFIA legacy project FEEDBACK that is currently mapping the [C II] 158 μm and the [O I] 63 μm fine structure lines in 11 Galactic star-forming regions with the upGREAT instrument. The [C II] line uniquely provides the kinematics of the gas exposed to the mechanical and radiative energy input by massive stars. By surveying regions with a range of massive star formation activity with stars of different spectral type, we will quantify the relationship between star formation activity and energy injection. We assess the negative (inhibition of star formation) and positive (triggering of star formation) feedback processes involved, and link that to other measures of activity on scales impacted by individual massive stars, small stellar groups, and star clusters. The [O I] line serves as a tracer for high density, high temperature PDRs and for shocks.

FEEDBACK takes full advantage of the unique capabilities of the upGREAT/SOFIA combination: The high spatial (14.1″) and spectral (0.2 km s^{-1}) resolution of the 14 pixel LFA upGREAT heterodyne spectrometer coupled with the nimble telescope of SOFIA allows for efficient mapping of the [C II] line over large (100's to 1000's of square arcmin) areas. With a total observing time of 96h, we will cover ~6700 arcmin^2 in the selected sources which are Cygnus X, M16, M17, NGC6334, NGC7538, RCW49, RCW79, RCW120, RCW36, W40, and W43. These [C II] maps, together with data for the less explored [O I] line, are delivered by the FEEDBACK consortium and are publically available. They provide a comprehensive database for the astronomical community and will serve as a starting point for many studies and follow-up observations.

This work is based on observations made with the NASA/DLR Stratospheric Observatory for Infrared Astronomy (SOFIA). SOFIA is jointly operated by the Universities Space Research Association, Inc. (USRA), under NASA contract NNA17BF53C, and the Deutsches SOFIA Institut (DSI) under DLR contract 50 OK 0901 to the University of Stuttgart. Financial support for the SOFIA Legacy Program, FEEDBACK, at the University of Maryland was provided by NASA through award SOF070077 issued by USRA.

We thank the USRA and NASA staff of the Armstrong Flight Research Center in Palmdale and of the Ames Research Center in Mountain View, and the Deutsches SOFIA Institut for their work on the observatory. We acknowledge the support by the upGREAT team for operating the instrument, for planning the detailed observing scenarios and in the calibration of the data. The development and operation of upGREAT was financed by resources from the MPI für Radioastronomie, Bonn, from Universität zu Köln, from the DLR Institut für Optische Sensorsysteme, Berlin, and by the Deutsche Forschungsgemeinschaft (DFG) within the grant for the Collaborative Research Center 956 as well as by the Federal Ministry of Economics and Energy (BMWI) via the German Space Agency (DLR) under Grants 50 OK 1102, 50 OK 1103 and 50 OK 1104.

The FEEDBACK project is supported by the BMWI via DLR, Projekt Number 50 OR 1916 (FEEDBACK) and Projekt Number 50 OR 1714 (MOBS—MOdellierung von Beobachtungsdaten SOFIA).

This work was also supported by the Agence National de Recherche (ANR/France) and the Deutsche Forschungsgemeinschaft (DFG/Germany) through the project "GENESIS" (ANR-16-CE92-0035-01/DFG1591/2-1).

Interstellar medium studies at Leiden Observatory are supported through a Spinoza award.

H.B. acknowledges support from the European Research Council under the Horizon 2020 Framework Program via the ERC Consolidator Grant CSF-648505. H.B. also acknowledges support from the DFG via SFB 881 "The Milky Way System" (sub-project B1).

ORCID iDs

N. Schneider https://orcid.org/0000-0003-3485-6678

References

Abdollahi, S., Acero, F., Ackermann, M., et al. 2020, ApJS, 247, 33
Ackermann, M., Ajello, M., Allafort, A., et al. 2011, Sci, 334, 1103
Aharonian, F., Akhperjanian, A. G., Bazer-Bachi, A. R., et al. 2007, A&A, 467, 3
Anderson, L. D., Bania, T. M., Balser, D. S., et al. 2011, ApJS, 194, 32
Anderson, L. D., Bania, T. M., Balser, D. S., et al. 2014, ApJS, 212, 18
Anderson, L. D., Deharveng, L., Zavagno, A., et al. 2015, ApJ, 800, 101
Anderson, L. D., Makai, Z., Luisi, M., et al. 2019, ApJ, 882, 11
Anderson, L. D., Zavagno, A., Barlow, M. J., et al. 2012, A&A, 537, 1
Anderson, L. D., Zavagno, A., Rodon, J., et al. 2010, A&A, 518, L99
André, P., Men'shchikov, A., Bontemps, S., et al. 2010, A&A, 518, 102
André, P., Reveret, V., Könyves, V., et al. 2016, A&A, 592, A54
Andree-Labsch, S., Ossenkopf-Okada, V., & Röllig, M. 2017, A&A, 598, 2
Baba, D., Nagata, T., & Nagayama, T. 2004, ApJ, 614, 818
Bakes, E. L. O., & Tielens, A. G. G. M. 1994, ApJ, 427, 822
Bally, J., Anderson, L., Battersby, C., et al. 2010, A&A, 518, L90
Balog, Z., Muzerolle, J., Rieke, G. H., et al. 2007, ApJ, 660, 1532
Beaumont, C. N., Goodman, A. A., Kendrew, S., et al. 2014, ApJS, 214, 18
Beaumont, C. N., & Williams, J. P. 2010, ApJ, 709, 791
Bertoldi, F. 1989, ApJ, 346, 735
Beuther, H., Tackenberg, J., Linz, H., et al. 2012, A&A, 538, 11
Brogan, C. L., Hunter, T. R., Cyganowski, C., et al. 2016, ApJ, 832, 187
Bykov, A. M., Ellison, D. C., Marcowith, A., et al. 2018, SSR, 214, 41
Cambrésy, L., Marton, G., Feher, O., Toth, L. V., & Schneider, N. 2013, A&A, 557, 29
Cantat-Gaudin, T., Jordi, C., Vallenari, A., et al. 2018, A&A, 618, A93
Carlhoff, P., Nguyen Luong, Q., Schilke, P., et al. 2013, A&A, 560, 24
Chaves, R. C. G., Renaud, M., Lemoine-Goumard, M., & Goret, P. 2008, in AIP Conf. Ser. 1085, Proc. of the 4th Int. Meeting on High Energy Gamma-Ray Astronomy (Melville, NY: AIP), 372
Chibueze, J. O., Omodaka, T., & Handa, T. 2014, ApJ, 784, 114
Churchwell, E., Povich, M. S., Allen, D., et al. 2006, ApJ, 649, 759
Comerón, F., Pasquali, A., G. Rodighiero, G., et al. 2002, A&A, 389, 874
Cubick, M., Stutzki, J., Ossenkopf, V., Kramer, C., & Roellig, M. 2008, A&A, 488, 623
Dagdigian, P. J. 2019, JCP, 151, 054306
Dale, D. A., & Helou, G. 2002, ApJ, 576, 159

Dale, J. E., Ngoumou, J., Ercolano, B., & Bonnell, I. A. 2014, MNRAS, 442, 694
Deharveng, L., Schuller, F., Anderson, L. D., et al. 2010, A&A, 523, A6
Deharveng, L., Zavagno, A., Schuller, F., et al. 2009, A&A, 496, 177
Dent, W. R. F., Hovey, G. J., Dewdney, P. E., et al. 2009, MNRAS, 395, 1805
Draine, B. T. 2011, ApJ, 732, 100
Elmegreen, B. G. 2011, EAS Publications Series, 51, 45
Elmegreen, B. G., & Lada, C. J. 1977, ApJ, 214, 725
Figueira, M., Zavagno, A., Deharveng, L., et al. 2017, A&A, 600, A93
Fissel, L., Ade, P. A. R., Angile, F. E., et al. 2019, ApJ, 878, 110
Frau, P., Girart, J. M., Zhang, Q., et al. 2014, A&A, 567, 116
Furukawa, N., Dawson, J. R., Ohama, A., et al. 2009, ApJL, 696, L115
Geen, S., Hennebelle, P., Tremblin, P., & Rosdahl, J. 2016, MNRAS, 463, 3129
Godard, B., Pineau des Forets, G., Lesaffre, P., et al. 2019, A&A, 622, 100
Goldsmith, P. F., Langer, W. D., Pineda, J. L., & Velusamy, T. 2012, ApJS, 203, 13
Graf, U., Simon, R., Stutzki, J., et al. 2012, A&A, 542, L16
Gritschneder, M., Burkert, A., Naab, T., & Walch, S. 2010, ApJ, 723, 971
Gritschneder, M., Naab, T., Walch, S., et al. 2009, ApJ, 694, L26
Guan, X., Stutzki, J., Graf, U., et al. 2012, A&A, 542, L4
Guarcello, M. G., Micela, G., Peres, G., et al. 2010, A&A, 521, 61
Güdel, M., Briggs, K. R., Montmerle, T., et al. 2008, Sci, 319, 309
Guevara, C., Stutzki, J., Ossenkopf-Okada, V., et al. 2020, A&A, 636, A16
Güsten, R., Nyman, L. A., Schilke, P., et al. 2006, A&A, 454, L13
Haid, S., Walch, S., Naab, T., et al. 2016, MNRAS, 460, 2962
Heays, A. N., Bosman, A. D., & van Dishoeck, E. F. 2017, A&A, 602, A105
Helou, G., Khan, I. R., Malek, L., & Boehmer, L. 1988, ApJS, 68, 151
Hennemann, M., Motte, F., Schneider, N., et al. 2012, A&A, 543, L3
Herbig, G. 1974, PASP, 86, 604
HESS Collaboration, Abramowski, A., Acero, F., et al. 2011, A&A, 525, 46
Hester, J. J., Scowen, P. A., Ankrit, R., et al. 1996, AJ, 111, 6
Hill, T., André, P., Arzoumanian, D., et al. 2012a, A&A, 548, L6
Hill, T., Motte, F., Didelon, P., et al. 2012b, A&A, 542, A114
Hollenbach, D., & McKee, C. F. 1989, ApJ, 342, 306
Hollenbach, D., & Tielens, A. G. G. M. 1999, RvMP, 71, 173
Hopkins, P. F., Keres, D., Onorbe, J., et al. 2014, MNRAS, 445, 581
Inutsuka, S., Inoue, T., Iwasaki, K., et al. 2015, A&A, 580, A49
Jayasinghe, T., Dixon, D., Povich, M. S., et al. 2019, MNRAS, 488, 1141

Joblin, C., Bron, E., & Pinto, C. 2018, A&A, 615, 129
Juarez, C., Girart, J. M., Zamora-Aviles, M., et al. 2017, ApJ, 844, 44
Kaufman, M., Wolfire, M. G., & Hollenbach, D. J. 2006, ApJ, 644, 283
Kim, J.-G., Kim, W.-T., & Ostriker, E. C. 2018, ApJ, 859, 68
Kirsanova, M., Pavlyuchenkov, Ya N., Wiebe, D. S., et al. 2019, MNRAS, 488, 5641
Klein, B., Hochgürtel, S., Krämer, I., et al. 2012, A&A, 542, L3
Könyves, V., André, P., Men'shchikov, A., et al. 2015, A&A, 584, A91
Kovalenko, A., Dung Tran, T., Rednyk, S., et al. 2018, ApJ, 856, 100
Krumholz, M. R., & Matzner, C. D. 2009, ApJ, 703, 1352
Kuhn, M. A., Hillenbrand, L. A., Sills, A., et al. 2019, ApJ, 870, 32
le Petit, F., Nehmé, C., le Bourlot, J., et al. 2006, ApJS, 164, 506
Lee, M. Y., Madden, S., le Petit, F., et al. 2019, A&A, 628, 113
Lefloch, B., & Lazareff, B. 1994, A&A, 289, 559
Lemoine-Goumard, M., Ferrara, E., Grondin, M.-H., Martin, P., Renauld, M., et al. 2011, MmSAI, 82, 739
Leurini, S., Wyrowski, F., Wiesemeyer, H., et al. 2015, A&A, 584, 70
Lique, F., Kłos, J., Alexander, M. H., et al. 2018, MNRAS, 474, 2313
Liu, H., Figueira, M., Zavagno, A., et al. 2017, A&A, 602, A95
Lopez, L. A., Krumholz, M. R., & Bolatto, A. D. 2011, ApJ, 731, 91
Lopez, L. A., Krumholz, M. R., & Bolatto, A. D. 2014, ApJ, 795, 121
Luisi, M., Anderson, L. D., Balser, D. S., Bania, T. M., & Wenger, T. V. 2016, ApJ, 824, 125
Mackey, J., Gvaramadze, V. V., Mohamed, S., & Langer, N. 2015, A&A, 573, A10
Maloney, P. R., Hollenbach, D. J., & Tielens, A. G. G. M. 1996, ApJ, 466, 561
Marston, A. P., Reach, W. T., Noriega-Crespo, A., et al. 2004, ApJS, 154, 333
Martins, F., Pomares, M., Deharveng, L., et al. 2010, A&A, 510, 32
Massi, F., Weiss, S., Elia, D., et al. 2019, A&A, 628, A110
Matzner, C. D. 2002, ApJ, 566, 302
McKee, C., & Ostriker, J. 1977, ApJ, 218, 148
Meijerink, R., Spaans, M., & Israel, F. P. 2006, ApJL, 650, L103
Meixner, M., Haas, M. R., & Tielens, A. G. G. M. 1992, ApJ, 390, 499
Meng, F., Sanchez-Monge, A., Schilke, P., et al. 2019, A&A, 630, 73
Miao, J., White, G. K., Thompson, M. A., & Nelson, R. P. 2009, ApJ, 692, 382
Minier, V., Tremblin, P., & Motte, F. 2013, A&A, 550, 50
Mizuta, A., Kane, J. O., Pound, M. W., et al. 2005, ApJ, 621, 803
Molinari, S., Swinyard, B., & Bally, J. 2010, A&A, 518, L100
Mookerjea, B., Ossenkopf, V., Ricken, O., et al. 2012, A&A, 542, L17
Mookerjea, B., Sandell, G., Güsten, R., et al. 2019, A&A, 626, 131
Mookerjea, B., Sandell, G., Vacca, W., et al. 2018, A&A, 616, 31
Moscadelli, L., Reid, M. J., Menten, K. M., et al. 2009, ApJ, 693, 406
Motte, F., Nguyen-Luong, Q., & Schneider, N. 2014, A&A, 571, 32
Motte, F., Schilke, P., Lis, D., et al. 2003, ApJ, 582, 277
Motte, F., Zavagno, A., Bontemps, S., et al. 2010, A&A, 518, L77
Nagy, Z., Choi, Y., Ossenkopf-Okada, V., et al. 2017, A&A, 599, 22
Neufeld, D. A., & Wolfire, M. G. 2016, ApJ, 826, 183
Ohja, D. K., Tamura, M., & Nakajima, Y. 2004, ApJ, 616, 1042
Okada, Y., Higgins, R., Ossenkopf-Okada, V., et al. 2019, A&A, 631, L12
Okada, Y., Pilleri, P., Berné, O., et al. 2013, A&A, 553, 2
Ortiz-León, G. N., Dzib, S. A., Kounkel, M. A., et al. 2017, ApJ, 834, 143
Ossenkopf, V., Koumpia, E., Okada, Y., et al. 2015, A&A, 580, 83
Ossenkopf, V., Röllig, M., Neufeld, D. A., et al. 2013, A&A, 550, 57
Pabst, C., Goicoechea, J. R., Teyssier, D., et al. 2017, A&A, 606, A29
Pabst, C., Goicoechea, J. R., Teyssier, D., et al. 2020, A&A, 639, 2
Pabst, C., Higgins, R., Goicoechea, J. R., et al. 2019, Nature, 565, 618
Padovani, M., Marcowith, A., Sanchez-Monge, A., et al. 2019, A&A, 630, 72
Paine, S. 2019, zenodo, doi:10.5281/zenodo.3406483
Paladini, R., Burigana, C., Davies, R. D., et al. 2003, A&A, 397, 213
Pellegrini, E. W., Baldwin, J. A., Brogan, C. L., et al. 2007, ApJ, 658, 1119
Pellegrini, E. W., Baldwin, J. A., Ferland, G. J., et al. 2011, ApJ, 738, 34
Peng, T.-C., Wyrowski, F., Zapata, L. A., et al. 2012, A&A, 538, 12
Peretto, N., André, P., Könyves, V., et al. 2012, A&A, 541, 63
Persi, P., & Tapia, M. 2008, Handbook of Star-forming Regions, Vol. II (San Francisco, CA: Astronomical Society of the Pacific), 456
Pound, M. W., Reipurth, B., & Bally, J. 2003, AJ, 125, 2108
Pound, M. W., & Wolfire, M. G. 2008, adass XVII, 394, 654
Puga, E., Marin-Franch, A., Najarro, F., et al. 2010, A&A, 517, 2
Rauw, G., Sana, H., & Nazé, Y. 2011, A&A, 535, A40
Reipurth, B., & Schneider, N. 2008, Handbook of Star-forming Regions, Vol. I (San Francisco, CA: Astronomical Society of the Pacific), 36
Risacher, C., Güsten, R., Stutzki, J., et al. 2016, A&A, 595, 34
Risacher, C., Güsten, R., Stutzki, J., et al. 2018, JAI, 4, 1840014
Röllig, M., Abel, N. P., Bell, T., et al. 2007, A&A, 467, 187
Röllig, M., Ossenkopf, V., Jeyakumar, S., et al. 2006, A&A, 451, 917
Roman-Zuniga, C. G., Elston, R., Ferreira, B., & Lada, E. 2008, ApJ, 672, 861
Russeil, D., Georgelin, Y. M., Amram, P., et al. 1998, AAPS, 130, 119
Russeil, D., Schneider, N., Anderson, L. D., et al. 2013, A&A, 554, A42
Russeil, D., Tigé, J., Adami, C., et al. 2016, A&A, 587, 135
Rygl, K. L. J., Brunthaler, A., Sanna, A., et al. 2012, A&A, 539, 79
Sadaghiani, M., Sanchez-Monge, A., Schilke, P., et al. 2020, A&A, 635, A2
Schneider, N., André, P., Könyves, V., et al. 2013, ApJL, 766, L17
Schneider, N., Bontemps, S., Motte, F., et al. 2016, A&A, 591, 40
Schneider, N., Bontemps, S., Simon, R., et al. 2006, A&A, 458, 855
Schneider, N., Csengeri, T., Bontemps, S., et al. 2010, A&A, 520, 49
Schneider, N., Csengeri, T., Hennemann, M., et al. 2012a, A&A, 540, L11
Schneider, N., Güsten, R., Tremblin, P., et al. 2012b, A&A, 542, L18
Schneider, N., Röllig, M., Simon, R., et al. 2018, A&A, 617, 45
Schneider, N., Stutzki, J., Winnewisser, G., et al. 1998, A&A, 338, 262
Schneps, M. H, Ho, P. T. P., & Barrett, A. H, 1980, ApJ, 240, 84
Shuping, R. Y., Vacca, W. D., Kassis, M., et al. 2012, AJ, 144, 116
Simpson, R. J., Povich, M. S., Kendrew, S., et al. 2012, MNRAS, 424, 2442
Spaans, M., & Meijerink, R. 2008, ApJL, 678, L5
Spitzer, L. 1968, Interscience Tracts on Physics and Astronomy (New York: Wiley)
Stock, D. J., Wolfire, M., Peeters, E., et al. 2015, A&A, 579, 67
Stroemgren, B. 1939, ApJ, 89, 526
Stutzki, J., Bensch, F., Heithausen, A., Ossenkopf, V., & Zielinksy, M. 1998, A&A, 336, 697
Stutzki, J., & Güsten, R. 1990, ApJ, 356, 513

Stutzki, J., Stacey, G. J., Genzel, R., et al. 1988, ApJ, 332, 379
Tatischeff, V., & Gabici, S. 2018, ARNPS, 68, 377
Thompson, M. A., Urquhart, J. S., Moore, T., et al. 2012, MNRAS, 421, 408
Tigé, J., Motte, F., Russeil, D., et al. 2017, A&A, 602, A77
Torii, K., Hasegawa, K., Hattori, Y., et al. 2015, ApJ, 806, 7
Townsley, L. K., Broos, P. S., Garmire, G. P., et al. 2014, ApJS, 213, 1
Townsley, L. K., Broos, P. S., Garmire, G. P., et al. 2018, ApJS, 235, 43
Townsley, L. K., Broos, P. S., Garmire, G. P., et al. 2019, ApJS, 244, 28
Tran, T. D., Rednyk, S., Kovalenko, A., et al. 2018, ApJ, 854, 25
Tremblin, P., Audit, E., Minier, V., et al. 2012a, A&A, 546, A33
Tremblin, P., Audit, E., Minier, V., & Schneider, N. 2012b, A&A, 538, A31
Tremblin, P., Minier, V., Schneider, N., et al. 2013, A&A, 560, A19
Tremblin, P., Schneider, N., Minier, V., Schmidt, W., & Schneider, N. 2014, A&A, 564, A106
Tsujimoto, M., Feigelson, E. D., Townsley, L. K., et al. 2007, ApJ, 665, 719
Vargas-Alvarez, C. A., Kobulnicky, H. A., Bradley, D. R., et al. 2013, AJ, 145, 125
Walch, S., Whitworth, A. P., Bisbas, T. G., Hubber, D. A., & Wuensch, R. 2015, MNRAS, 452, 2794
Walch, S., Whitworth, A. P., Bisbas, T. G., Wuensch, R., & Hubber, D. A. 2013, MNRAS, 435, 917
Walch, S., Whitworth, A. P., Girichidis, P., et al. 2012, MNRAS, 419, 760
Watkins, E. J., Peretto, N., Marsh, K., et al. 2019, A&A, 628, 21
Weaver, R., McCray, R., Castor, J., et al. 1977, ApJ, 218, 377
White, G., Lefloch, B., Fridlund, C. V. M., et al. 1997, A&A, 323, 931
Whiteoak, J. B. Z., & Uchida, K. I. 1997, A&A, 317, 563
Williams, J. P., de Geus, E. J., & Blitz, L. 1994, ApJ, 428, 693
Williams, R. J. R., Ward-Thompson, D., & Whitworth, A. P. 2001, MNRAS, 327, 788
Wilson, T. L., Hanson, M. M., & Muders, D. 2003, ApJ, 590, 895
Wolfire, M. G., Hollenbach, D., & McKee, C. F. 1995, ApJ, 443, 152
Wolfire, M. G., Hollenbach, D., & McKee, C. F. 2010, ApJ, 716, 1191
Wolfire, M. G., McKee, C. F., Hollenbach, D., & Tielens, A. G. G. M. 2003, ApJ, 587, 278
Wright, N., Drake, J., Drew, J. E., et al. 2012, ApJ, 746, L21
Wright, N., Drew, J. E., & Mohr-Smith, M. 2015, MNRAS, 449, 741
Wu, Y., Reid, M., Dame, T., et al. 2019, ApJ, 874, 94
Xu, J., Zavagno, A., Yu, N., et al. 2019, A&A, 627, 27
Zavagno, A., Anderson, L. D., Russeil, D., et al. 2010, A&A, 518, L101
Zavagno, A., André, P., Schuller, F., et al. 2020, A&A, 638, 7
Zavagno, A., Pomares, M., Deharveng, L., et al. 2010, A&A, 472, 835
Zeidler, P., Sabbi, E., Nota, A., et al. 2015, AJ, 150, 78
Zernickel, A., Schilke, P., Smith, R., et al. 2013, A&A, 554, L2
Zhang, B., Moscadelli, L., Sato, M., et al. 2014, ApJ, 781, 89
Zhang, S., Zavagno, A., Yuam, J., et al. 2020, A&A, 637, A40